White Rose Research Online

eprints@whiterose.ac.uk
https://eprints.whiterose.ac.uk
Universities of Leeds, Sheffield and York

Deposited via The University of Sheffield.

White Rose Research Online URL for this paper:
https://eprints.whiterose.ac.uk/id/eprint/244841/

Version: Accepted Version

Article:
Teksin, B.A., Sezer, H.N., Çamlıca, F.B. et al. (2026) Investigation of the room- and low-temperature performance of resistance-welded CF/PEKK joints: effects of welding time and double-welding. Composites Part A: Applied Science and Manufacturing, 210. 110126. ISSN: 1359-835X

https://doi.org/10.1016/j.compositesa.2026.110126

© 2026 The Authors. Except as otherwise noted, this author-accepted version of a journal article published in Composites Part A: Applied Science and Manufacturing is made available via the University of Sheffield Research Publications and Copyright Policy under the terms of the Creative Commons Attribution 4.0 International License (CC-BY 4.0), which permits unrestricted use, distribution and reproduction in any medium, provided the original work is properly cited. To view a copy of this licence, visit http://creativecommons.org/licenses/by/4.0/

Reuse
This article is distributed under the terms of the Creative Commons Attribution (CC BY) licence. This licence allows you to distribute, remix, tweak, and build upon the work, even commercially, as long as you credit the authors for the original work. More information and the full terms of the licence here: https://creativecommons.org/licenses/

Takedown
If you consider content in White Rose Research Online to be in breach of UK law, please notify us by emailing eprints@whiterose.ac.uk including the URL of the record and the reason for the withdrawal request.

UNIVERSITY OF LEEDS
University of Sheffield
UNIVERSITY of York

Investigation of the Room- and Low-Temperature Performance of Resistance-Welded CF/PEKK Joints: Effects of Welding Time and Double-Welding

Buse Atac Teksin[a,b,c], Halil Nezih Sezer[d], Fahri Buğra Çamlıca[d], Levent Civan[d], Hatice S. Sas[a,b,c,*]

[a] School of Mechanical, Aerospace and Civil Engineering, The University of Sheffield, S1 3JD, UK

[b] Faculty of Engineering and Natural Sciences, Sabanci University, Orhanli-Tuzla, 34956, Istanbul, Turkey

[c] Integrated Manufacturing Technologies Research and Application Center, Sabanci University, Orhanli-Tuzla, 34956, Istanbul, Turkey

[d] TAI, Turkish Aerospace Industries, Kazan, Ankara, Turkey

* Corresponding author: Hatice S. Sas, email: h.s.sas@sheffield.ac.uk

ABSTRACT

This study examined the combined influence of welding time, double-welding (DW), and service temperature on the integrity and mechanical performance of resistance-welded CF/PEKK joints. A DW methodology was introduced and evaluated as an additional processing route for the purpose of joint re-activation, rework, and reconsolidation. A resistance-welding processing window was established through thermal characterisation to enable controlled melting and crystallisation. Single- and double-welded joints produced at different heating-stage durations were assessed by optical microscopy, micro-CT, post-weld comparative crystallinity analysis, single-lap shear testing at room temperature and −50 °C, and dynamic mechanical analysis. Increasing welding time improved consolidation, reduced voids, and increased room-temperature lap-shear strength in single-welded joints. DW improved joint quality at shorter welding times; however, at longer welding times, it reduced room-temperature strength despite lower void content, indicating welding-cycle-dependent changes in the post-weld state. At −50 °C, both joint types exhibited higher strength and a more brittle response, with behaviour governed primarily by matrix stiffening rather than porosity differences. The results demonstrate that the performance of resistance-welded CF/PEKK joints is controlled by the combined effects of welding time, the second welding cycle, and service temperature. Double-welding, therefore, introduces an additional processing degree of freedom to improve robustness in resistance-welded CF/PEKK joints.

Keywords: CF/PEKK; Resistance welding; Thermoplastic welding; Low-temperature performance

1. Introduction

Thermoplastic composites are increasingly used in aerospace structures because of their high specific mechanical performance, manufacturing flexibility, and re-melting capability, which enables welding, repair, and rework [1]. Since large or geometrically complex composite structures often require joining, the reliability of the joint is critical to structural efficiency and long-term performance [2, 3]. For thermoplastic composites, welding is particularly attractive compared with mechanical fastening and adhesive bonding because it can reduce added mass, avoid drilling-induced stress concentrations, and minimise extensive surface preparation [4, 5].

Resistance welding (RW) is a practical joining route for large-scale thermoplastic composite structures, including aerospace components, because it combines localised heating with relatively simple hardware and short cycle times [6, 7]. In RW, an electrically resistive heating element (HE), commonly a metal mesh or carbon-based heater, is placed at the overlap interface and supplied with current to generate heat by Joule heating. The resulting temperature rise brings the interfacial polymer above its glass transition temperature (Tg) or melting temperature (Tm), enabling melt flow under pressure, intimate contact, and interfacial healing, followed by consolidation on cooling [7, 8]. In practice, current delivery is achieved via a power supply and electrical clamping, while insulation and pressure application are used to limit heat loss and promote through-thickness consolidation; therefore, joint formation is governed by the coupled control of electrical input and applied pressure [9]. A schematic of the RW configuration and heating-element placement is shown in Figure 1. Marti et al. [10] described this process in a four-stage sequence: heating, melting, crystallisation, and cooling, where a controlled reduction in electrical input during the crystallisation stage promotes gradual cooling and stabilises interfacial crystallisation, thereby reducing the risk of uncontrolled microstructural development. Achieving a repeatable temperature–time profile across these stages is therefore critical for robust welding and is governed primarily by the current level, heating-stage duration (welding time), and applied pressure, which have been widely examined in the literature [11-13]. In practice, suitable parameter windows are commonly established via preliminary welding trials and/or finite element modelling of the thermal field.

Figure 1. Schematic representation of a typical resistance welding setup.

The quality of resistance-welded joints is strongly influenced by local thermal and melt-flow conditions within the joint region. Void formation is a recognised challenge in the thermal processing of thermoplastic

composites [14]. In resistance-welded joints, voids may arise from incomplete interfacial melt-flow, trapped air, or non-uniform temperature distribution, particularly in complex heating element architectures. Such residual porosity can reduce load transfer efficiency and influence joint mechanical performance, highlighting the need to mitigate void formation to improve process control and weld integrity [15].

Among the governing parameters, welding time is particularly critical because it controls the duration of heat input and therefore the interfacial thermal exposure that drives melting, interdiffusion, and consolidation. Modelling work by Panneerselvam et al. [16] highlighted its significance, attributing approximately 20% of the overall contribution to weld performance to welding time in resistance-welded GF/PP joints. For a given current level, increasing welding time increases the energy delivered to the interface and elevates the interfacial temperature, which must be high enough to fully melt the matrix yet remain below the onset of thermally driven damage mechanisms [17]. Experimental studies consistently report an optimum window: lap-shear strength increases with welding time until sufficient melting/healing is achieved, then declines under prolonged exposure, as shown for GF/PEI and CF/PEEK systems by Shi et al. [18] and Shen et al. [19]. Similar behaviour was reported by Cheng et al. [20] for GF/PP, where short durations produced incomplete melting while extended heating promoted microstructural deterioration, leading to a peak strength at an intermediate welding time. In addition, insufficient welding time can restrict melt flow and hinder evacuation of trapped air, increasing porosity within the weld region during solidification [21]. Collectively, these results indicate that welding time must be tuned to balance interfacial melting/healing and consolidation against degradation risks. However, despite extensive work on other thermoplastic composite systems, the specific role of welding time in resistance-welded CF/PEKK joints has not yet been systematically established.

Aircraft structures operate across a wide service-temperature envelope and may experience sub-zero environments down to approximately −50 °C [22]. Such temperature variations can significantly affect the mechanical response and durability of joined composite components through changes in matrix stiffness, interfacial behaviour, and stress redistribution within the overlap [23]. Although the temperature dependence of adhesively bonded and mechanically fastened composite joints has been extensively studied [24-26], comparatively fewer investigations have addressed welded thermoplastic joints, particularly resistance-welded configurations [27, 28]. Koutras et al. [29] examined GF/PPS resistance-welded joints and reported a non-linear dependence of joint performance on temperature, including increased strength at

−50 °C accompanied by changes in failure behaviour and load transfer within the overlap. Shen et al. [19] showed that resistance-welded CF/PEEK joints exhibit strong temperature sensitivity, with increasing service temperature reducing lap-shear strength and altering dominant failure modes at the weld interface. However, despite these contributions, systematic investigations of the low-temperature mechanical performance of resistance-welded CF/PEKK joints remain limited. This gap is particularly relevant given the growing uptake of CF/PEKK in aerospace structures, where robust processing windows and reliable joint performance under sub-zero service conditions are required.

Accordingly, this study established a framework linking processing conditions, weld-region structure, and mechanical performance for resistance-welded CF/PEKK single-lap joints with two specific aims. First, the influence of heating-stage duration (welding time) on the weld thermal history, consolidation/porosity evolution, post-weld crystallinity, and lap-shear performance was quantified, and joint performance was further evaluated at −50 °C to reflect sub-zero service conditions. Second, a double-welding approach was introduced for the first time in literature, in which the joint was re-activated through a second resistance-welding cycle after initial welding and cooling. This processing route creates a distinct cumulative thermal history from a single uninterrupted weld, enabling the effect of a second thermal cycle on melt flow, interfacial healing, porosity reduction, reconsolidation, and mechanical performance to be examined. By linking thermal history, weld-region structure, and temperature-dependent mechanical response, the study clarifies the processing conditions governing the performance of resistance-welded CF/PEKK joints and evaluates double-welding as an additional processing variable alongside conventional single-weld optimisation.

2. Materials and Experimental Methods

2.1. Materials

In this study, high-temperature-resistant Toray Cetex® TC1320 CF/PEKK unidirectional tape (Toray Advanced Composites, USA) was used to manufacture a composite laminate, which served as adherends for resistance welding. The tape had 34% resin content, a fibre areal weight (FAW) of 145 g/m², and a prepreg areal weight (PAW) of 221 g/m² [30].

CF/PEKK composite adherends were joined by resistance welding using a multi-layered heating element (HE) consisting of a glass fibre (GF) ply, a neat thermoplastic polymer film, and stainless steel (SS) metal mesh. A plain-woven E-glass fabric (GW110P, METYX Composites) with a FAW of 110 g/m² and a

nominal thickness of 0.02 mm was used as the insulating layer. A neat polyether ether ketone (PEEK) polymer film (Victrex, UK) with a thickness of 0.08 mm and a glass transition temperature (T_g) of 143 °C was selected to create a resin-rich interlayer that fills the open gaps within the metal mesh, and melts together with the composite adherends during welding. PEEK was selected as a practical PAEK-based interlayer film because it is commercially available in suitable film form, can impregnate the open mesh architecture during hot pressing/welding, and has a processing temperature range compatible with the PEKK adherend matrix. The compatibility of the PEEK film with the PEKK matrix was subsequently assessed by DSC using a PEKK–PEEK blend.

The resistive heating component was an SS mesh with a thickness of 0.1 mm, a wire diameter of 50 μm, and an open-gap width of 90 μm. During welding, electrical current was supplied to the mesh to generate heat via Joule heating.

2.2. Resistance Welding Operation

2.2.1. Manufacturing of CF/PEKK Composite Adherends

Cross-ply CF/PEKK laminates were manufactured with a stacking sequence of $[0/90]_{5s}$ using hot compression moulding, following the processing route reported by Elmas et al. [31]. Before lay-up, Loctite Frekote 700-NC release agent was applied to both steel press plates and allowed to dry for 20 min. A perforated polyimide release film (UPILEX® 25S) was placed on the lower plate to facilitate laminate removal. The laminate dimensions were set to 600 mm × 600 mm to match the resistance-welding setup requirements. After the lay-up, the stack was covered with a release film, and the upper plate was positioned on top. The laminate was heated from room-temperature to 380 °C under 1 bar. A dwell time of 30 min was then applied at 380 °C under 10 bar. Cooling to room-temperature was carried out at 7 °C/min while maintaining 10 bar. After consolidation, adherends measuring 560 mm × 30 mm were sectioned from the laminate using a KUKA KR-16-2 CF robotic waterjet system [22].

2.2.2. Preparation of the Multi-Layered Heating Element

The constituents of the HE was stacked sequentially to form the multi-layered architecture (Figure 2.a). To promote wetting of the glass-fibre (GF) ply, the polymer film was placed adjacent to the GF layer, as shown in Figure 2.b. In addition, two layers of the PEEK film were positioned on both sides of the stainless-steel mesh to impregnate the mesh openings and generate a resin-rich interlayer during welding. Prior to welding, the assembled HE was pre-consolidated by hot pressing. The stack was heated to 380 °C under 2 bar,

followed by consolidation at 7 bar for 30 min, and then cooled to room-temperature under pressure. The consolidated HE was manufactured as a single sheet and subsequently cut into strips for resistance welding (see fabrication steps in Figure S1). The HE strips were 610 mm long (including 20 mm extensions at each end for electrical connection) and 30 mm wide. The final thickness of the consolidated strips was 0.67 ± 0.05 mm.

Figure 2. a) Schematic of the multi-layered HE positioned between the CF/PEKK adherends; b) architecture of the fabricated multi-layered HE.

2.2.3. The Application of the Welding Process

The resistance welding setup in Figure 3 is designed with a unique structure for industrial applications, incorporating a DC power supply system (maximum 50 V and 200 A), clamping unit, a pneumatic pressure system, thermocouples for temperature monitoring, insulating blocks, and a post-weld cooling system. Electrical connections were established at both ends of the HE, using clamps to deliver current from the power supply. The insulating block, actuated by the pneumatic system, was pressed at 8 bar to facilitate contact between the composite adherends and to minimise undesired heat loss. The setup was designed for resistance welding of full-length composite adherends and was configured in the present study for specimens with dimensions of 560 mm × 30 mm.

Figure 3. Resistance-welding setup configuration

Figure 4 demonstrates the preparation of the welding stack before the resistance welding. The CF/PEKK composite adherends (560 mm x 30 mm) were assembled with the HE strips (610 mm × 30 mm), with the 20 mm mesh overhang at both ends serving as current entry/exit points. Because the setup was configured for full-length strip welding, standard SLS specimens were not welded individually. Instead, the overlap regions for SLS testing were predefined during stack preparation using polyimide release films, and the welded strips were sectioned after welding. The remaining central region of each welded strip was reserved for complementary characterisation, including optical microscopy, micro-CT, DSC, and DMA, as illustrated in Figure S2. This specimen allocation enabled both mechanical testing and detailed weld-quality assessment to be performed from the same welded strip, although the destructive nature of the tests prevented all analyses from being conducted on the identical local region. Therefore, during assembly, the overlap region required by the test standard was defined by placing the release film outside the intended

overlap area (Figure 4.b). Thermocouples were positioned within the welding stack (Figure 4.c) to record the joint-region temperature in real time.

Figure 4. Preparation stages of the welding stack: a) components of the welding stack; b) placement of release film to define overlap regions; c) thermocouple placement.

Based on pilot welding trials used to establish the processing window, a current of 50 A was applied during the heating stage to bring the PEKK matrix and PEEK film into the melt state by Joule heating. The current was then reduced to 40 A for 20 s (melting stage) to maintain the melt state, followed by 20 A for 100 s (crystallisation stage) to promote controlled, approximately isothermal cooling and to mitigate rapid crystallisation at the interface [10]. Power was then switched off for the cooling stage, and the stack remained clamped until the coupon temperature dropped below the T_g. The applied pressure was maintained at 8 bar throughout the welding cycle.

To investigate the effects of heating-stage duration (defined as welding time in this study) and a second welding cycle (double-welding) on joint quality, the heating-stage duration was varied between 50 s, 70 s, and 90 s. A subset of coupons was subjected to a second welding cycle using the same parameters as the first. The single-welded series therefore provided the reference response to increasing heating-stage duration, while the corresponding double-welded series isolated the effect of re-activating the joint through a second thermal cycle after cooling. Coupons welded once and twice are referred to as single-welded (SW) and double-welded (DW), respectively. The welding parameter sets are summarised in Table 1.

Table 1. Resistance welding parameters for different welding configurations.

2.3. Experimental Procedure

2.3.1. Quality Assurance of CF/PEKK Adherends

The density of the CF/PEKK laminate was measured in accordance with ASTM D792/Method A using water buoyancy based on Archimedes' principle. Void content and fibre volume content were determined using ASTM D3171/Method B via acid digestion. For this purpose, three specimens (30 mm x 30 mm) were prepared and tested. Void content was calculated using Eq. (1) [32]:

$$V_v = 100 - (V_f + V_m)$$

$$V_f = \frac{M_f}{M_i} x \frac{\rho_i}{\rho_f} x100 \qquad [1]$$

$$V_m = \frac{M_i - M_f}{M_i} x \frac{\rho_i}{\rho_m} x100$$

where V_f, V_m, and V_v are the volumetric fractions (%) of fibres, matrix, and voids, respectively. M_i and M_f denote the specimen mass (g) before and after digestion; and ρ_f, ρ_m, and ρ_i are the densities (g/cm³) of the fibres, matrix, and the sample, respectively.

Laminate quality was further assessed by optical microscopy (Nikon LV100ND). For cross-sectional examination, specimens were mounted in epoxy and polished to obtain a flat, scratch-free surface suitable for microstructural inspection [33].

2.3.2. Thermal Characterisation

Differential scanning calorimetry (DSC) was performed in three measurement sets: (i) CF/PEKK adherends and the PEEK film used in the HE, to define the thermal process window by determining the T_g, T_m, crystallisation behaviour (T_c), and degree of crystallinity (X_c); (ii) a PEKK–PEEK blend to assess adherend–HE compatibility via T_g; and (iii) polymer bleed-out collected from the overlap region of welded joints, representative of the molten polymer expelled during welding, to evaluate process-induced changes in thermal behaviour and comparative crystallinity and to provide insight into the thermal history experienced during welding. All DSC measurements were performed using the Mettler Toledo DSC+3 under an inert nitrogen (N_2) atmosphere (50 mL/min). The analyses were conducted over a temperature range of 25°C to 400°C at a heating/cooling rate of 10°C/min [34]. The calculation of the degree of crystallinity (X_c) is given in Eq. (2) as:

$$X_c(\%) = \frac{\Delta H_m}{\Delta H_m^{\circ}(1 - W_f)} x100 \quad [2]$$

where ΔH_m is the measured melting enthalpy, ΔH_m° is the melting enthalpy of fully crystalline PEKK (130 J/g) [35], and W_f is the fibre weight fraction in the composite laminate.

For the compatibility assessment (set ii), the PEKK–PEEK blend was prepared by combining PEEK film with CF/PEKK such that the mass of the PEKK matrix matched the mass of the PEEK film (1.857 mg PEEK film and 5.457 mg CF/PEKK, based on a 34 wt% matrix content for the tape [30, 36]. For the welded-joint assessment (set iii), polymer bleed-out was collected by carefully removing the resin extruded from the overlap region after welding and analysed by DSC. Although the bleed-out does not represent the full weld-zone microstructure, it provides a practical, fibre-free proxy for comparing welding-cycle-dependent thermal history and crystallisation behaviour between conditions. As the bleed-out material was assumed to be fibre-free, W_f was set to zero for crystallinity calculations using Eq. (2).

The thermogravimetric analysis (TGA) was carried out to examine the thermal degradation of the CF/PEKK adherend and the neat PEEK film. TGA measurements were conducted using a Mettler Toledo TGA-DSC+3 from 25°C to 1000°C at a heating rate of 10°C/min under a nitrogen (N_2) atmosphere.

2.3.3. Structural Integrity Assessment of Welded Adherends

Micro X-ray computed tomography (micro-CT) was performed using a Phoenix V|tome|x M 300/180 system (Waygate Technologies, Germany) to characterise the voids in the welding region and identify defects in the adherend and joint area arising from manufacturing and/or welding [24]. The system consists of an X-ray generator, detector, rotatable sample control system, data analysis unit, and 3D reconstruction module. Scans were conducted at an accelerating voltage of 160 kV and a tube current of 120 μA. The voxel size was 20 μm, and no filters were applied during scanning. The CT datasets were post-processed utilising Datos|x (v2.14.0) and VGSTUDIO MAX (2023.1). Analyses focused on the central section remaining after the removal of single-lap shear (SLS) specimens from the 560 mm long welding coupon (Figure S2.a). All CT specimens measured 25 mm x 40 mm x 6.6 mm. For quantitative analysis, regions of interest (ROI) measuring 25 mm x 25 mm x 2.5 mm were defined, and void analysis was performed using the same ROI volume for all conditions. In addition, optical microscopy was used for cross-sectional examination of the welded joints (Nikon LV100ND) following the procedure given in Section 2.3.1.

2.3.4. Comprehensive Characterisation of Temperature-Dependent Mechanical Behaviour

Joining performance was evaluated by Single-lap shear (SLS) testing following the procedures of ASTM D5868 standard [37], focusing on the effects of heating-stage duration (welding time) and the application of a second welding cycle (double-welding). Welded adherends (560 mm × 30 mm) were sectioned into SLS specimens of 101 mm × 30 mm, with the specimen width constrained by the resistance-welding setup configuration (Section 2.2.3). All specimens were tested using a crosshead speed of 13 mm/min, following the standard loading procedure. For each welding configuration and test temperature, two independently welded coupons were produced (Figure S2.b), resulting in four SLS specimens per welding configuration at each test temperature. During cutting, polyimide release film regions introduced during welding (Figure 4.b, c) were used to define a 30 mm × 30 mm welded area, while the upper and lower portions of the adherends outside the overlap were removed (Figure S2.c). All cutting operations were carried out with the Tongtai TMV-1050QII CNC machine.

Tabbing material was cut from the same CF/PEKK laminate used to manufacture the adherends. To achieve effective tabbing, the sample surfaces were roughened using sandpaper, the adhesive film (Scotch-Weld AF 163–2 K, 3M) was applied between the tabbing material and lap shear specimens, and the tabbed samples were left to cure for a day to allow proper bonding. This procedure finalised the SLS specimen preparation (Figure 5.a). Lap-shear specimens representing six different welding configurations (Table 1) were tested on an Instron 5982 Universal Testing Machine (Figure 5.b, c) at 13 mm/min. In addition to testing at room -temperature (22°C), SLS tests were performed at -50°C to assess low-temperature joint performance. An environmental conditioning chamber (Figure 5.d, e) was integrated into the test frame and cooled to -50°C under a nitrogen (N_2) atmosphere, with a 30 min conditioning period before testing. To account for transient heat influx when opening the chamber door during specimen installation, the chamber temperature was allowed to re-stabilise at -50°C before each test (Figure 5.f). Following SLS testing, fracture surfaces were examined by visual inspection to identify the dominant failure features across welding conditions.

Figure 5. The single-lap shear test: a) some samples before the test; b-c) SLS fixture; d-e) the sample inside the environmental conditioning chamber; f) the temperature monitoring of the chamber.

2.3.5. Dynamic Mechanical Analysis (DMA)

Dynamic mechanical analysis (DMA) was performed to characterise the temperature-dependent viscoelastic response of the welded CF/PEKK joints and to isolate the effect of the second welding cycle under the highest-performing welding condition. Based on the weld-quality and lap-shear results, DMA was conducted on SW90 and DW90 joints only, as these conditions exhibited the most continuous interfaces and lowest void contents, thereby minimising compliance artefacts and premature damage during dual-cantilever loading while enabling a controlled comparison at a fixed heating-stage duration.

DMA specimens (55 mm × 13 mm) were sectioned from the welded coupons to include the welded overlap region. Testing was carried out using a Mettler Toledo DMA1 in dual cantilever mode. The test configuration followed ASTM D7028-07, and the dual-cantilever fixture/setup was applied in accordance with ASTM D4065. Temperature sweeps were conducted over −50 °C to 250 °C and 25 °C to 250 °C to capture the low-temperature and elevated-temperature mechanical response of the welded joints. For the −50 °C to 250 °C programme, specimens were held briefly at −50 °C at the start of the test to ensure thermal equilibrium prior to heating. A heating rate of 3 °C/min and a frequency of 1.0 Hz were used for all measurements. Each condition was tested in duplicate to confirm repeatability.

Figure S3 summarises the experimental programme, organised into four strands: (i) CF/PEKK laminate quality assurance; (ii) pre-welding thermal characterisation to define the resistance-welding process window; (iii) CF/PEKK–heating-element compatibility assessment; and (iv) weld-quality evaluation.

3. Results and Discussion

3.1. Laminate Quality

Laminate density and constituent volume fractions were evaluated following the procedures described in Section 2.3.1. Using the supplier-reported fibre and matrix densities (1.79 g/cm³ and 1.3 g/cm³, respectively), the CF/PEKK laminate exhibited V_f and V_m of 59.04% and 40.46%, respectively, corresponding to a void content of 0.5%. The measured laminate density, ρ_c, was 1.5829 g/cm³. Thus, the porosity level remained below 1%, confirming that the hot-press consolidation route produced a high-quality laminate suitable for subsequent resistance-welding trials [38, 39]. Consistent with these quantitative results, optical microscopy was used to examine the laminate microstructure and void distribution. Representative cross-sectional micrographs at 25× and 50× magnification (Figure S4) show a homogeneous laminate architecture with no visually apparent void clusters, indicating effective consolidation. As microscopy interrogates a localised region of interest, it may not capture sparsely distributed defects when the bulk void content is as low as 0.5%; nevertheless, the images are consistent with the low porosity measured from the volumetric analysis.

3.2. Determination of the Process Window Through Preliminary Analyses

The DSC results for the CF/PEKK adherend and the PEEK film used in the HE (Section 2.3.2, set i) are shown in Figure 6 and summarised in Table 2. From the heating curves (Figure 6.a), the T_g values of CF/PEKK and PEEK of the HE were 156.01°C and 151.68°C, respectively. The corresponding T_m values were 334.11°C (CF/PEKK) and 342.50°C (PEEK). From the cooling curves (Figure 6.b), the peak crystallisation temperatures, $T_{c,peak}$ were 278.05 °C for CF/PEKK and 294.83 °C for PEEK in the HE. In addition to $T_{c,peak}$, the crystallisation ranges were determined as 295.56°C to 219.41°C for CF/PEKK and 305.68°C to 273.14°C for PEEK in the HE. These ranges were used to define the post-heating (crystallisation) stage of the resistance-welding cycle, where reduced electrical input promotes controlled, approximately isothermal crystallisation at the joint interface [10]. Finally, using the melting enthalpies and Eq. (2), the degree of crystallinity (X_c) values were calculated as 27.91% and 27.23% for CF/PEKK and

PEEK in the HE, respectively. These values provide reference points for interpreting crystallinity changes in the welded joints and for assessing the influence of welding parameters on joint formation and quality.

Figure 6. DSC thermograms of CF/PEKK and PEEK of the heating element: a) second heating, b) cooling.

Thermal stability was assessed by TGA (Figure 7). The onset of detectable mass loss occurred at 532.16 °C for the PEEK film (99.5% mass retained) and at 556.35 °C for CF/PEKK (99% mass retained) (Table 2). By 1000 °C, the total mass loss reached 50.36% for PEEK and 12.45% for CF/PEKK. The higher residual mass of CF/PEKK is attributable to the presence of carbon fibres and their reported influence on the apparent thermal stability/char yield of polymer systems [40]. Although both materials show negligible mass loss up to 530 °C, rapid high-temperature processing can activate degradation mechanisms; therefore, a conservative maximum allowable temperature was adopted for the welding process.

Figure 7. TGA curves of CF/PEKK and PEEK in the heating element.

Table 2. DSC and TGA results of CF/PEKK and PEEK in the heating element.

Based on the DSC- and TGA-derived thermal limits (Table 2), a resistance-welding processing window was defined to ensure complete melting and bonding while enabling controlled crystallisation and avoiding thermal degradation. The heating stage was therefore constrained to 360–450 °C (Table 3), i.e., above the measured melting temperatures of both CF/PEKK and the PEEK-containing HE, while remaining below the conservative upper temperature limit. To achieve this heating range, a peak current of 50 A was applied during the heating stage. A subsequent crystallisation stage was implemented by reducing the current to 20 A for 100 s, maintaining the joint temperature within 300–220 °C to promote controlled crystallisation, corresponding to the crystallisation temperature window determined by DSC. In addition, a conservative maximum allowable welding temperature of 500 °C was adopted based on TGA results. Pilot welding trials were used to select heating-stage durations and welding pressure, as summarised in Section 2.2.3. The resulting processing window and parameter set are summarised in Table 3.

Table 3. Processing window adapted for resistance welding.

Following the process parameters given in Table 1, temperature–time profiles were recorded for each welding condition using thermocouples positioned in the overlap region (Figure 4.c). Representative thermal histories for all welding conditions are provided in Figure S5. Across all conditions, the applied current levels resulted in characteristic thermal profiles comprising a heating stage, a short melting stage, a

crystallisation stage, and a cooling stage. Particularly relevant to the subsequent thermal profiles, the crystallisation stage (20 A for 100 s) maintained the joint temperature within the DSC-defined crystallisation window (300–220 °C; Table 3), providing suitable conditions for controlled and uniform crystallisation prior to cooling. The overall thermal histories were consistent in terms of the imposed crystallisation-stage conditions, which form the basis for interpreting the process-induced comparative crystallinity trends discussed in Section 3.4.2.

3.3. Adherend-Heating Element Compatibility Assessment

Compatibility between the PEKK matrix and the PEEK polymer in the HE, relevant to fusion bonding at the weld interface, was assessed by DSC analysis (Section 2.3.2, set ii). The PEKK–PEEK blend exhibited a single T_g at approximately 153.49 °C (Figure 8), positioned between the T_g values of CF/PEKK (156.01 °C) and the PEEK film (151.68 °C). The presence of a single T_g is consistent with compatibility within the amorphous phase, supporting the use of PEEK as an interlayer film in the heating element and indicating that polymer–polymer interaction between the PEEK film and PEKK matrix can occur during resistance welding [41].

Figure 8. DSC thermogram of the PEKK–PEEK blend prepared from CF/PEKK and the PEEK film in the heating element.

3.4. Welding Quality

The welding quality was assessed using thermal monitoring, microstructural inspection (optical microscopy and micro-CT), thermal analysis (DSC), mechanical testing (SLS), and dynamic mechanical analysis (DMA) (Figure S3).

3.4.1. Microstructural Inspection of Welded Joints

The effect of welding time and double-welding on joint integrity was examined by optical microscopy and micro-CT. Figure S6 shows the consolidated HE prior to welding. The thickness of the HE was 0.67 mm (Figure S6.a), and the measured wire diameter and mesh opening were 56.28 μm and 85.25 μm, respectively (Figure S6.b). No voids were observed in the consolidated HE, indicating effective pre-consolidation and a structurally sound interlayer architecture.

The cross-sectional micrographs of single-welded samples welded at 50 s, 70 s, and 90 s are shown in Figure 9. First, SW50 exhibited extensive voiding within the HE region together with incomplete interfacial bonding (Figure 9.a). Despite reaching elevated temperatures during the heating stage (Figure S5), the 50

s heating duration did not provide sufficient time for sustained melt flow and resin redistribution within the layered HE. Consequently, void evacuation from the GF weave and mesh openings was limited and interfacial healing remained incomplete. The absence of a continuous bonded interface further indicates that the thermal exposure was insufficient for time-dependent chain interdiffusion/reptation after intimate contact [15]. Moreover, localised deconsolidation was observed. This behaviour is attributed to stress relaxation in cross-ply laminates during secondary thermal cycles (such as welding), where residual stresses arising from the coefficient of thermal expansion (CTE) mismatch during manufacturing may be partially released. Under conditions of relatively high viscosity and limited matrix flow, this can manifest as ply separation despite the applied pressure [42, 43] . With increasing welding duration, deconsolidation was suppressed. SW70 showed improved interfacial contact relative to SW50; however, voiding remained pronounced, indicating that the additional thermal exposure was still insufficient to fully impregnate/fill the multi-layered HE architecture (Figure 9.b). In contrast, SW90 exhibited a more continuous interface and substantially reduced voiding (Figure 9.c), reflecting enhanced resin flow at higher temperature/longer exposure and the resulting improvement in consolidation and interfacial healing.

Figure 9. The cross-sectional area investigation through optical microscopy of single-welded samples: a) SW50; b) SW70; c) SW90.

The optical micrographs of the double-welded stacks are presented in Figure 10 which shows that the second welding cycle produced a clear improvement in joint consolidation. Relative to SW50, DW50 showed a reduction in voiding within the heating element region and a more continuous interface (Figure 10.a); the ply-level deconsolidation observed in SW50 was no longer apparent. This behaviour is consistent with the re-melting capability of thermoplastics, where reheating promotes additional resin flow and redistribution within the GF weave and mesh openings, facilitating void migration/mitigation and reconsolidation of thermally deconsolidated regions [44]. A similar trend was observed for the 70 s condition: compared with SW70, DW70 exhibited reduced voiding, indicating enhanced resin infiltration of the heating element architecture (Figure 10.b). Nevertheless, local interfacial discontinuities persisted, suggesting that despite improved bonding, interfacial healing between the adherend and HE remained incomplete under this parameter set. The most uniform and well-bonded microstructure was obtained for DW90 (Figure 10.c). After two consecutive 90 s cycles, the interface appeared largely continuous with minimal residual porosity, and the polymer-rich interlayer showed effective fusion with the adherend matrix

(consistent with the higher thermal exposure recorded during welding; Figure S5), promoting interfacial healing and consolidation. Hence, among the double-welded conditions, DW90 provided the highest joint quality at the microstructural level, combining strong interfacial bonding with virtually void-free consolidation (Figure 10.c).

Figure 10. The cross-sectional area investigation through optical microscopy of double-welded samples: a) DW50; b) DW70; c) DW90.

Micro-CT was used to quantify voids and other internal defects and to visualise their three-dimensional distribution within the weld region (Section 2.3.3) (for SW in Figure 11 and for DW in Figure 12). Owing to the layered HE and limited contrast between polymer-rich regions and surrounding features, segmentation of the weld interface is not always straightforward; in particular, unfilled mesh openings can appear as gaps in the reconstructed volume. For the single-welded joints (Figure 11), the deconsolidation observed optically in SW50 (Figure 9.a) was also evident in the CT slices (Figure 11.a). A progressive reduction in voiding was observed as welding time increased from 50 s to 90 s, with the 3D void maps shifting from red-dominant regions (larger void volumes) in SW50 and SW70 towards a blue–green scale (smaller void volumes) in SW90. Quantitatively (Figure 13), void content decreased from 4.80% (SW50) to 3.21% (SW70) and 1.75% (SW90), while the maximum void volume decreased from 48.63 mm^3 and 44.02 mm^3 (SW50 and SW70) to 21.23 mm^3 (SW90). These trends are consistent with the optical observations (Figure 9) and confirm that longer heating duration improves consolidation and reduces voiding within the joint region.

For the double-welded joints (Figure 12), voiding was generally reduced relative to the corresponding single-welded conditions, consistent with the microscopy results (Figure 10). Void content decreased from 4.80% to 2.94% for SW50 to DW50 and from 3.21% to 2.32% for SW70 to DW70 (Figure 13). The most pronounced improvement with double-welding was observed for the 90s condition: although void content decreased modestly from 1.75% (SW90) to 1.46% (DW90), the maximum void volume dropped sharply from 21.23 mm^3 to 1.81 mm^3 (91.47% reduction). This indicates that the second welding cycle was particularly effective in suppressing large, isolated void clusters. In summary, micro-CT and optical microscopy show consistent trends: increasing welding time and applying a second welding cycle enhance melt flow and infiltration within the multi-layered heating element, thereby reducing voids and improving the uniformity of the weld region. Moreover, the thermocouples were used to monitor representative

temperature–time histories and verify that the welding cycle remained within the defined processing window; full-field temperature mapping of the entire interface was not performed. Therefore, the spatial uniformity of the welded region was assessed after welding through optical microscopy and micro-CT analysis of interfacial continuity, consolidation quality, and void distribution.

Figure 11. Micro-CT slices and 3D void maps of single-welded composite adherends: a) SW50; b) SW70; c) SW90.

Figure 12. Micro-CT slices and 3D void maps of double-welded composite adherends: a) DW50; b) DW70; c) DW90.

Figure 13. Quantitative void metrics extracted from micro-CT for all welding conditions.

3.4.2. Post-Weld Thermal Behaviour and Crystallinity

Post-weld DSC measurements were performed on polymer bleed-out collected from the overlap region (Section 2.3.2, set iii), representative of the molten polymer expelled from the joint during welding, to evaluate process-induced changes in thermal response and comparative crystallinity. The DSC analysis results for both heating and cooling cycles are presented in Figure 14, and the extracted parameters are summarised in Table 4. Across all conditions, T_g, T_m, and T_c show only minor variations, with no consistent dependence on heating-stage duration or the application of a second welding cycle. These small shifts are within the expected sensitivity limits associated with the analysis of small bleed-out masses, which represent polymer bleed-out from the weld region rather than the constrained joint interface; thus, the discussion focuses on changes in the degree of crystallinity (X_c).

The resistance-welding cycle included a reduced-current (crystallisation) stage (20 A for 100 s) to maintain the joint within the DSC-defined crystallisation window (Table 3). As the heating-stage duration (welding time) increased, the joint reached higher peak temperatures and subsequently stabilised at higher isothermal holding temperatures during the 20 A/100s crystallisation stage (Figure S5), rising from 239 °C for SW50 to 291 °C for SW90. This shift in thermal history is reflected in the post-weld DSC results, where X_c increased monotonically from 25.34% (SW50) to 29.27% (SW70) and 31.60% (SW90) (Table 4). The higher isothermal holding temperatures at longer welding durations are expected to accelerate crystallisation kinetics and promote greater crystal development within the fixed 100 s stage, consistent with enhanced chain mobility at elevated temperatures [45], providing a process–structure link for the single-welded joints. Although the bleed-out does not quantify the absolute crystallinity of the constrained

interface, it provides a consistent comparative indicator of process-induced crystallisation trends across welding conditions.

Within the limitations of analysing the bleed-out material, the double-welded condition showed a different crystallinity response from the single-welded trend. DW50 exhibited a higher X_c than SW50 (30.18% vs. 25.34%; Table 4), despite a slightly lower crystallisation-stage holding temperature (228 °C vs. 239 °C; Figure S5). This suggests that the second thermal cycle enhanced crystal development, likely by increasing effective thermal exposure through repeated melt–recrystallisation and providing additional opportunity for nucleation and growth during the controlled crystallisation stage. In contrast, at longer heating durations, double welding did not increase crystallinity: DW70 and DW90 yielded X_c values of 29.13% and 28.86%, respectively (Table 4), corresponding to a negligible decrease relative to SW70 (−0.47%) and a more pronounced reduction relative to SW90 (−8.67%). Notably, DW90 experienced repeated exposure to high temperatures (Figure S5), which may promote thermo-oxidative degradation even in the absence of measurable mass loss in TGA [46]. In this regime, chain scission can reduce effective chain length, while oxidative crosslinking can restrict molecular mobility; both mechanisms can inhibit lamellar thickening and limit further crystallisation during subsequent cooling/holding [47, 48]. Accordingly, the reduction in X_c for DW70–DW90 is attributed to the competing influence of repeated high-temperature exposure, where degradation-related molecular changes offset the potential crystallisation benefit of a second welding cycle, despite the controlled crystallisation stage being retained in the process. These DSC results are therefore used as a comparative metric of process-dependent thermal history, rather than as a direct measurement of weld-interface crystallinity.

Figure 14. DSC thermograms of polymer bleed-out collected from the overlap region after resistance welding: a.1) second heating profile of SWs; a.2) cooling profile of SWs; b.1) second heating profile of DWs; b.2) cooling profile of DWs.

Table 4. Post-weld DSC results (polymer bleed-out) and crystallisation-stage holding temperatures for single-welded and double-welded joints.

3.4.3. Comprehensive Characterisation of Temperature-Dependent Mechanical Behaviour

Single-lap shear (SLS) responses of the resistance-welded CF/PEKK joints are summarised in Figure 15 for room-temperature (RT; Figure 15.a) and low temperature (LT; −50 °C; Figure 15.b), with the corresponding lap-shear strengths reported in Figure 15.c. Under RT conditions, the single-welded (SW)

joints show a strong dependence on heating-stage duration: the lap-shear strength increased from 4.78 MPa (SW50) to 6.06 MPa (SW70) and 17.11 MPa (SW90). This trend is consistent with the progressively improved consolidation and interfacial continuity observed by optical microscopy and micro-CT (Section 3.4.1). In particular, SW90 exhibited the most continuous interface and the lowest void content among the SW conditions (Figure 9.c and Figure 11.c), supporting its markedly higher load-carrying capacity. This behaviour is in line with resistance-welding literature on thermoplastic composites, where longer thermal exposure improves melt flow within the interlayer, promotes void evacuation under pressure, and increases interfacial healing once intimate contact is established [49, 50].

For the DW joints, the influence of the second cycle depended on the baseline heating time. At the shortest heating duration, double-welding increased RT strength from 4.78 MPa (SW50) to 6.37 MPa (DW50), consistent with thermoplastic re-melting enabling additional resin redistribution and reconsolidation within the multi-layered heating element [44]. By contrast, at longer heating durations the mechanical response did not scale directly with void reduction. Although DW90 exhibited strong consolidation and a pronounced reduction in maximum void volume in the joint region (Section 3.4.1), its RT strength (14.30 MPa) remained below SW90 (17.11 MPa). This divergence is consistent with the post-weld DSC trend (Section 3.4.2), which reflects comparative crystallinity of the bleed-out polymer due to the process-induced changes, and with reports that repeated high-temperature exposure can modify post-weld morphology and may initiate early-stage degradation reactions even below the decomposition threshold, which reduces comparative crystallinity and consequently compromises the mechanical performance of the polymer matrix [27, 51]. The load–displacement response further supports this interpretation, with DW90 exhibiting lower displacement at peak load, indicative of reduced deformability associated with restricted chain mobility and consistent with a more brittle mechanical response. A similar effect was more pronounced for the 70 s condition, where RT strength decreased from 6.06 MPa (SW70) to 3.27 MPa (DW70), indicating that the second cycle can be detrimental when the additional thermal history outweighs the benefits of further void mitigation and joint interface refinement.

At −50 °C, the SLS strengths increased for most configurations and the DW joints exceeded their SW counterparts at each welding time (Figure 15.c): DW50 increased to 9.23 MPa relative to SW50 (4.11 MPa), while smaller gains were observed for DW70 (6.47 MPa vs. 6.30 MPa) and DW90 (18.56 MPa vs. 18.38 MPa). The general strengthening at LT is consistent with reduced molecular mobility and increased matrix

stiffness, which can elevate apparent shear resistance and promote a more efficient stress transfer across the bonded region [52]. The limited sensitivity of the 90 s condition to a second cycle at −50 °C is also consistent with both SW90 and DW90 already exhibiting comparatively consolidated, low-void weld regions (Section 3.4.1), such that LT behaviour becomes governed more by the stiffened polymer response than by further incremental changes in porosity [53].

Fracture-surface observations (Figure 16) supported the trends identified in Sections 3.4.1–3.4.2. At room temperature, the lower-strength joints (SW50 and SW70) showed failure dominated by interfacial debonding, with minor interlaminar failure within the multi-layered heating element, indicating incomplete interfacial fusion at shorter heating durations. This behaviour is consistent with the discontinuous interfaces and higher void contents observed by optical microscopy and micro-CT. With increasing heating-stage duration, the dominant failure mode progressively shifted from interfacial debonding towards more internally disruptive damage. SW90 exhibited interlaminar failure accompanied by localised composite separation and mesh tearing, indicating that improved fusion and load transfer shifted the limiting mechanism from a weak interface towards damage within the heating-element architecture and adjacent laminate. SW90 exhibited interlaminar failure accompanied by localised composite separation and mesh tearing, indicating that improved fusion shifted the limiting mechanism from a weak interface toward damage within the heating element architecture and adjacent laminate [25]. This transition is consistent with the failure-mode framework discussed by Stavrov and Bersee ~~[4]~~, where interfacial failure is associated with imperfect bonding, whereas interlaminar failure is generally associated with improved weld quality.

For the double-welded joints, DW50 still showed regions described as weakly bonded, alongside more pronounced interlaminar failure, suggesting that the second cycle improved consolidation but did not fully remove local interface discontinuities at the shortest heating time. In contrast, the higher-duration double-welded joints showed more extensive internal damage. DW90 exhibited the most severe interlayer disruption, with mesh tearing at room-temperature, consistent with a more brittle fracture response despite its lower displacement at peak load, and combined glass-fibre and mesh tearing at −50 °C. DW70 also exhibited mesh tearing, particularly at −50 °C. Overall, fracture surfaces at low-temperature appeared more abrupt and locally brittle, with more pronounced tearing in the stronger joints, consistent with reduced polymer ductility of the interlayer. This interpretation is consistent with SEM observations reported by

Yildirim et al. [25], who showed that low-temperature exposure in CF/PEKK bonding systems promotes polymer embrittlement, leading to interfacial debonding and even fibre-dominated fracture, thereby supporting the fracture behaviour observed in the present study.

Figure 15. Single-lap shear test results of single-welded and double-welded samples: a) room-temperature (RT) tests; b) -50°C (LT) tests; c) single-lap shear strength values.

Figure 16. The fracture surfaces of single-welded and double-welded samples after single-lap shear test under RT and LT.

3.4.4. Dynamic Mechanical Response (DMA)

Figure 17 presents the DMA temperature-sweep responses of SW90 and DW90, selected based on their higher joint quality and mechanical performance in the preceding assessments (Sections 3.4.1 and 3.4.3). Sweeps were performed from 25 °C (RT) to 250 °C and from −50 °C to 250 °C to examine the influence of starting temperature on the viscoelastic response.

For the RT-start tests, DW90 exhibited a consistently higher storage modulus (E′) than SW90 across the measured temperature range, with onset values of 5.46 GPa and 3.62 GPa, respectively (Figure 17.a), indicating a stiffer joint response under dynamic loading. Notably, this increased stiffness did not translate into higher RT lap-shear strength, as DW90 remained weaker than SW90 in SLS (Section 3.4.3). This decoupling suggests that the second welding cycle altered the joint structure and/or interface in a manner that increased dynamic stiffness but did not improve resistance to static failure, consistent with reports that repeated high-temperature exposure can modify welded interfaces and shift failure behaviour towards a more brittle fracture response in thermoplastic composite joints [27]. The damping response further supported this interpretation: DW90 exhibited a lower tan(δ) peak than SW90 (Figure 17.b), indicating reduced damping and more restricted molecular mobility in the welded region after the second cycle, consistent with standard DMA interpretations of tan(δ) in semi-crystalline thermoplastic systems [54]. As the DSC results indicated only minor changes in thermal response, the glass transition temperature was further assessed using DMA, which is known to provide greater sensitivity to viscoelastic transitions and temperature-dependent mechanical properties [55, 56] . Consistent with this, both joints exhibited similar T_g values, in agreement with the minimal differences observed in DSC measurements (Table 4).

Starting the sweep at −50 °C produced only modest changes in E′ for both joints (Figure 17.c), indicating that the stiffness ranking between SW90 and DW90 was not strongly affected by the initial conditioning

step. Similarly, tan δ trends remained comparable between RT-start and −50-start tests (Figure 17.d), with only minor differences in peak magnitude/shape. In summary, the DMA results show that the welded joints' viscoelastic response reflected their thermal history (single- vs double-welding), and they complement the temperature-dependent SLS behaviour by highlighting that increased stiffness (higher E′) does not necessarily imply increased lap-shear strength for these joints.

Figure 17. DMA temperature sweeps of resistance-welded CF/PEKK joints (SW90 and DW90): a) storage modulus, E′, RT-start; b) tan(δ), RT-start; c) storage modulus, E', −50 °C-start; d) tan(δ), −50 °C-start.

4. Conclusion

This study systematically examined how heating-stage duration (welding time), a second welding cycle (double-welding), and service temperature influenced the structural integrity and mechanical performance of resistance-welded CF/PEKK joints. Increasing welding time improved interfacial consolidation and reduced void content, which corresponded to substantial gains in room-temperature lap-shear strength for single-welded joints. These results confirmed that sufficient thermal exposure was necessary to promote melt flow, intimate contact, and interfacial healing within the weld region.

The effect of double-welding depended on the baseline thermal condition. At shorter heating durations, the second cycle promoted re-melting and reconsolidation, improving joint integrity and increasing lap-shear strength. At longer heating durations, however, double-welding reduced room-temperature strength despite lower void content and improved interfacial continuity. This divergence indicated that additional consolidation did not necessarily translate into higher static performance when repeated thermal exposure modified the post-weld polymer state, as reflected by the comparative crystallinity trends derived from the bleed-out DSC analysis. Consistent with this interpretation, double-welded joints exhibited higher stiffness and altered damping behaviour in DMA, suggesting increased molecular constraint following the second welding cycle.

Low-temperature testing (−50 °C) revealed a distinct shift in governing behaviour. Joint strengths increased for both single- and double-welded configurations and the response became more brittle. Under these conditions, performance was dominated by matrix stiffening and reduced molecular mobility, and sensitivity to porosity variations diminished for the higher-quality joints. Fracture-surface observations

supported these trends, showing more abrupt failure features and more pronounced disruption within the heating-element architecture in the higher-performing joints at low temperature.

Future work should define processing limits for cumulative thermal exposure during re-welding and clarify the mechanisms by which repeated cycles modify PEKK morphology and room-temperature strength, with the aim of preserving reconsolidation benefits without compromising static performance. In addition, the double-welding concept suggests a practical pathway for rework/repair of resistance-welded thermoplastic composite joints by re-activating the embedded heating element; dedicated studies should therefore quantify repair effectiveness, repeatability, and property retention after one or more re-welding cycles under representative service conditions.

5. Acknowledgement

This research did not receive any specific grant from funding agencies in the public, commercial, or not-for-profit sectors.

6. References

[1] Reis JP, de Moura M, Samborski S. Thermoplastic Composites and Their Promising Applications in Joining and Repair Composites Structures: A Review. Materials (Basel). 2020;13(24):5832–.
[2] Siddique A, Iqbal Z, Nawab Y, Shaker K. A review of joining techniques for thermoplastic composite materials. Journal of Thermoplastic Composite Materials. 2023;36(8):3417–54.
[3] Shi H. Resistance welding of thermoplastic composites Process and performance: Technische Universiteit Delft; 2014.
[4] Stavrov D, Bersee HEN. Resistance welding of thermoplastic composites-an overview. Composites Part A: Applied Science and Manufacturing. 2005;36(1):39–54.
[5] Barroeta Robles J, Dubé M, Hubert P, Yousefpour A. Repair of thermoplastic composites: an overview. Advanced Manufacturing: Polymer & Composites Science. 2022;8(2):68–96.
[6] Choudhury MR, Debnath K. A review of the research and advances in electromagnetic joining of fiber-reinforced thermoplastic composites. Polymer Engineering and Science. 2019;59(10):1965–85.
[7] Shi H, Villegas IF, Bersee HEN. A displacement-detection based approach for process monitoring and processing window definition of resistance welding of thermoplastic composites. Composites Part A: Applied Science and Manufacturing. 2015;74:1–9.
[8] Dubé M, Hubert P, Gallet JNAH, Stavrov D, Bersee HEN, Yousefpour A. Metal mesh heating element size effect in resistance welding of thermoplastic composites. Journal of Composite Materials. 2012;46(8):911–9.
[9] Wei D, Gu Y, Zhu H, Li M, Wang S. Influence of Electrical Heating Metal Mesh and Power Density on Resistance Welding of Carbon Fiber/PEEK Composite. Polymers. 2022;14(13).
[10] Marti IB, Kaynak C. Effects of interlayer forms on the resistance welding performance of PAEK/CF thermoplastic composite laminates. Journal of Thermoplastic Composite Materials. 2023;36(12):4945–76.
[11] Ageorges C, Ye L, Hou M. Experimental investigation of the resistance welding for thermoplastic-matrix composites. Part I: heating element and heat transfer. Composites Science and Technology. 2000;60(7):1027–39.
[12] Ageorges C, Ye L, Hou M. Experimental investigation of the resistance welding of thermoplastic-matrix composites. Part II: optimum processing window and mechanical performance. Composites Science and Technology. 2000;60(8):1191–202.
[13] Hou M, Ye L, Mai YW. An Experimental Study of Resistance Welding of Carbon Fibre Fabric Reinforced Polyetherimide (CF Fabric/PEI) Composite Material. Applied Composite Materials. 1999;6(1):35–49.

[14] Shi H, Villegas IF, Bersee HEN. Analysis of void formation in thermoplastic composites during resistance welding. Journal of Thermoplastic Composite Materials. 2017;30(12):1654–74.
[15] Totla HS, Gupta A, Mishra S, Sharma S, Selvaraj SK. Resistance welding analysis of thermoplastic composite structures in aeronautical applications. International Journal on Interactive Design and Manufacturing. 2023.
[16] Panneerselvam K, Aravindan S, Noorul Haq A. Study on resistance welding of glass fiber reinforced thermoplastic composites. Materials and Design. 2012;41:453–9.
[17] Geng Z, Yu S, Wang S, Tian Z, Gao Z, Wang K, et al. Advances in Resistance Welding of Fiber-Reinforced Thermoplastics. Materials. 2024;17(19).
[18] Shi H, Fernandez Villegas I, Bersee H. Effect of Fibre-matrix Adhesion and Fibre Orientation on Thermoplastic Composite Welded Joints. SAMPE 2013 Conference. California, USA2013. p. 1–15.
[19] Shen L, Zhang Y, Zhang H, Sun M, Jian X, Xu J. Strength evaluation of CF/PEEK resistance welding based on improved artificial neural network: Interface failure mechanism study under extreme service temperatures. Composites Part B: Engineering. 2025;297.
[20] Cheng X, Su G, Du B, Long W, Liu J, Feng T, et al. Resistance welding process for glass fiber-reinforced polypropylene composite joints: Parameter optimization and performance assessment. Polymer Composites. 2025;46(11):10376–88.
[21] Zhang Y, Shen L, Fan X, Yan Z, Xiao J, Jian X, et al. Enhanced comprehension of the cross-scale forming mechanism in CF/PEEK resistance welding: Analysis of temperature gradients and meso–microscopic phase transitions. Composites Part B: Engineering. 2024;283.
[22] Seyyednourani M, Akgun S, Ulus H, Yildiz M, Sas HS. Experimental investigation on Compression-After-Impact (CAI) response of aerospace grade thermoset composites under low-temperature conditions assisted with acoustic emission monitoring. Composite Structures. 2023;321:117260–.
[23] Adams RD, Coppendale J, Mallick V, Al-Hamdan H. The effect of temperature on the strength of adhesive joints. International Journal of Adhesion and Adhesives. 1992;12(3):185–90.
[24] Seyednourani M, Akgun S, Ulus H, Yildiz M, Sas HS. Impact damage and low temperature effects on carbon fiber/epoxy joints: A comparative study of hybrid bolted/bonded and bolted configurations with cross-ply and angle-ply laminates. Composites Part A: Applied Science and Manufacturing. 2025;190.
[25] Yildirim C, Ulus H, Sas HS, Topal S, Yildiz M. Assessing the fracture and dynamic mechanical performance of CF/PEKK joints bonded with epoxy-based adhesive film for aerospace applications: Impact of thermal and cycling hygrothermal conditions. Composites Part A: Applied Science and Manufacturing. 2025;190.
[26] Ashcroft IA, Hughes DJ, Shaw SJ, Wahab MA, Crocombe A. Effect of Temperature on the Quasi-static Strength and Fatigue Resistance of Bonded Composite Double Lap Joints. The Journal of Adhesion. 2001;75(1):61–88.
[27] Rohart V, Lebel LL, Dubé M. Effects of environmental conditions on the lap shear strength of resistance-welded carbon fibre/thermoplastic composite joints. Composites Part B: Engineering. 2020;198.
[28] Hu C, Gui S, Xu R, Wang W, Fu Z, Ji W. Effects of moisture and temperature on shear strength of resistance welded joints of CF/PEEK composites. Journal of Thermoplastic Composite Materials. 2025;39(1):323–43.
[29] Koutras N, Villegas IF, Benedictus R. Influence of temperature on the strength of resistance welded glass fibre reinforced PPS joints. Composites Part A: Applied Science and Manufacturing. 2018;105:57–67.
[30] Toray. Toray Cetex ® TC1320 PEKK PRODUCT DATA SHEET. 2019;31(0):1–3.
[31] Elmas S, Atac B, Al-Nadhari A, Topal S, Yildiz M, Sas HS. Mitigating drilling-induced damage and hot-wet aging effects through reconsolidation in CF/PEKK composites. Journal of Thermoplastic Composite Materials. 2025;38(12):4640–67.
[32] Elkolali M, Nogueira LP, Rønning PO, Alcocer A. Void Content Determination of Carbon Fiber Reinforced Polymers: A Comparison between Destructive and Non-Destructive Methods. Polymers. 2022;14(6).
[33] Karimi S, Louyeh PY, Barzegar A, Yildiz M, Sas HS. A study of post-processing for AFP-fabricated thermoplastic composites with void content and air permeability characterization. Journal of Reinforced Plastics and Composites. 2023;43(9-10):490–503.
[34] Barzegar A, Karimi S, Sukur EF, Sas HS, Yildiz M. Effect of fiber orientation on temperature history during laser-assisted thermoplastic fiber placement. Journal of Reinforced Plastics and Composites. 2022;42(17-18):953–68.

[35] Quiroga Cortés L, Caussé N, Dantras E, Lonjon A, Lacabanne C. Morphology and dynamical mechanical properties of poly ether ketone ketone (PEKK) with meta phenyl links. Journal of Applied Polymer Science. 2016;133(19):1–10.
[36] Grünewald J. Thermoplastic composite sandwiches for structural helicopter applications. 2018.
[37] ASTM D5868-2014. Standard Test Method for Lap Shear Adhesion for Fiber Reinforced Plastic (FRP) Bonding. West Conshohocken, PA, USA2014.
[38] Zhang D, Heider D, Gillespie JW. Void reduction of high-performance thermoplastic composites via oven vacuum bag processing. Journal of Composite Materials. 2017;51(30):4219–30.
[39] Saenz-Castillo D, Martín MI, Calvo S, Rodriguez-Lence F, Güemes A. Effect of processing parameters and void content on mechanical properties and NDI of thermoplastic composites. Composites Part A: Applied Science and Manufacturing. 2019;121(March):308–20.
[40] Gaitanelis D, Worrall C, Kazilas M. Detecting, characterising and assessing PEEK's and CF-PEEK's thermal degradation in rapid high-temperature processing. Polymer Degradation and Stability. 2022;204.
[41] Barzegar A, Karimi S, Sas HS, Yildiz M. Enhancing interlaminar bonding quality estimation in laser-assisted fiber placement of CF/PEKK composites: A correction factor approach for improved prediction of intimate contact. Composites Part A: Applied Science and Manufacturing. 2024;181(February):108095–.
[42] Parlevliet PP, Bersee HEN, Beukers A. Residual stresses in thermoplastic composites-A study of the literature-Part I: Formation of residual stresses. Composites Part A: Applied Science and Manufacturing2006. p. 1847–57.
[43] Shokrieh MM, Safarabadi M. Understanding residual stresses in polymer matrix composites. Residual Stresses in Composite Materials: Elsevier; 2021. p. 217–45.
[44] Lu M, Ye L, Mai Y-W. Thermal de-consolidation of thermoplastic matrix composites—II. "Migration" of voids and "re-consolidation". Composites Science and Technology. 2004;64(2):191–202.
[45] Jin L, Ball J, Bremner T, Sue HJ. Crystallization behavior and morphological characterization of poly(ether ether ketone). Polymer. 2014;55(20):5255–65.
[46] McLauchlin AR, Ghita OR, Savage L. Studies on the reprocessability of poly(ether ether ketone) (PEEK). Journal of Materials Processing Technology. 2014;214(1):75–80.
[47] Horikx MM. Chain scissions in a polymer network. Journal of Polymer Science. 2003;19(93):445–54.
[48] Gaitanelis D, Chanteli A, Worrall C, Weaver PM, Kazilas M. A multi-technique and multi-scale analysis of the thermal degradation of PEEK in laser heating. Polymer Degradation and Stability. 2023;211.
[49] Xiong X, Wang D, Wei J, Zhao P, Ren R, Dong J, et al. Resistance welding technology of fiber reinforced polymer composites: a review. Journal of Adhesion Science and Technology. 2021;35:1593–619.
[50] Brassard D, Dubé M, Tavares JR. Resistance welding of thermoplastic composites with a nanocomposite heating element. Composites Part B: Engineering. 2019;165(January):779–84.
[51] Ma Xl, Wen Lh, Wang Sy, Xiao Jy, Li Wh, Hou X. Inherent relationship between process parameters, crystallization and mechanical properties of continuous carbon fiber reinforced PEEK composites. Defence Technology. 2023;24:269–84.
[52] Nikonovich M, Costa JFS, Fonseca AC, Ramalho A, Emami N. Structural, thermal, and mechanical characterisation of PEEK-based composites in cryogenic temperature. Polymer Testing. 2023;125.
[53] Kim Y-H, Kumar S, Li X, Kim S-Y, Shin D-H. Temperature-dependent mechanical properties and material modifications of carbon fiber composites for optimized structures in high-end industrial applications. Composites Part B: Engineering. 2025;303.
[54] Hopmann C, Dahlmann R, Weihermüller M, Wipperfürth J, Sommer J. Determination of the frequency- and temperature-dependent stiffness and damping properties of thermoplastics for the prediction of the vibration and heating behaviour during ultrasonic welding. Welding in the World. 2022;67(2):435–45.
[55] Sukur EF, Elmas S, Eskizeybek V, Sas HS, Yildiz M. An experimental implication of long-term hot-wet-aged carbon fiber/polyether ketone ketone composites: The impact of automated fiber placement process parameters and process-induced defects. Journal of Applied Polymer Science. 2023;140(29).
[56] Sukur EF, Elmas S, Seyyednourani M, Eskizeybek V, Yildiz M, Sas HS. A rational study on the hydrothermal aging of AFP manufactured CF/polyetherketoneketone composites with in situ consolidation supported by acoustic emission inspection. Journal of Applied Polymer Science. 2022;139(29):1–14.

Table 1. Resistance welding parameters for different welding configurations.

Sample Name	Welding Repetition	Heating Stage		Melting Stage		Crystallization Stage		Cooling Stage
		Welding Time (s)	Electrical Current (A)	Welding Time (s)	Electrical Current (A)	Welding Time (s)	Electrical Current (A)	Electrical Current (A)
SW50	1	50	50	20	40	100	20	0
SW70	1	70	50	20	40	100	20	0
SW90	1	90	50	20	40	100	20	0
DW50	2	50	50	20	40	100	20	0
DW70	2	70	50	20	40	100	20	0
DW90	2	90	50	20	40	100	20	0

Table 2. DSC and TGA results of CF/PEKK and PEEK in the heating element.

	DSC							TGA	
	T_g (°C)	T_m (°C)	T_c (°C)			ΔH_m (J/g)	X_c (%)	T_d (°C)	Mass Loss (%)
			Onset	Peak	Endset				
CF/PEKK	156.01	334.11	295.56	278.05	219.41	12.06	27.91	556.35	12.45
Multi-layered HE	151.68	342.50	305.68	294.83	273.14	35.41	27.23	532.16	50.36

Table 3. Processing window adapted for resistance welding.

Welding Time (Heating)	Welding Current (Heating)	Welding Current/Time (Crystallization)	Welding Pressure	Heating Temperature Range	Cooling Temperature Range	Maximum Allowable Temperature
50-70-90 s	20-50A	20A-100s	8 bar	360-450°C	300-220°C	500°C

Table 4. Post-weld DSC results (polymer bleed-out) and crystallisation-stage holding temperatures for single-welded and double-welded joints.

	T_g (°C)	T_m (°C)	T_c (°C)	ΔH_m (J/g)	X_c (%)	Isothermal Crystallization Holding Temperature (°C)
SW50	147.87	342.17	295.17	32.95	25.34	239
SW70	149.7	343	294.5	38.06	29.27	284
SW90	149.39	341.83	294.17	42.25	31.6	291
DW50	150.35	342.17	295.17	39.24	30.18	228
DW70	151.29	342.17	293.5	37.88	29.13	231
DW90	148.97	341.83	295.17	37.52	28.86	276

List of Figures

Figure 1. Schematic representation of a typical resistance welding setup.

Figure 2. a) Schematic of the multi-layered HE positioned between the CF/PEKK adherends; b) architecture of the fabricated multi-layered HE.

Figure 3. Resistance welding setup configuration.

Figure 4. Preparation stages of the welding stack: a) components of the welding stack; b) placement of release film to define overlap regions; c) thermocouple placement.

Figure 5. The single-lap shear test: a) some samples before the test; b-c) SLS fixture; d-e) the sample inside the environmental conditioning chamber; f) the temperature monitoring of the chamber.

Figure 6. DSC thermograms of CF/PEKK and PEEK of the heating element: a) second heating, b) cooling.

Figure 7. TGA curves of CF/PEKK and PEEK in the heating element.

Figure 8. DSC thermogram of the PEKK–PEEK blend prepared from CF/PEKK and the PEEK film in the heating element.

Figure 9. The cross-sectional area investigation through optical microscopy of single-welded samples: a) SW50; b) SW70; c) SW90.

Figure 10. The cross-sectional area investigation through optical microscopy of double-welded samples: a) DW50; b) DW70; c) DW90.

Figure 11. Micro-CT slices and 3D void maps of single-welded composite adherends: a) SW50; b) SW70; c) SW90.

Figure 12. Micro-CT slices and 3D void maps of double-welded composite adherends: a) DW50; b) DW70; c) DW90.

Figure 13. Quantitative void metrics extracted from micro-CT for all welding conditions.

Figure 14. DSC thermograms of polymer bleed-out collected from the overlap region after resistance welding: a.1) second heating profile of SWs; a.2) cooling profile of SWs; b.1) second heating profile of DWs; b.2) cooling profile of DWs.

Figure 15. Single-lap shear test results of single-welded and double-welded samples: a) room-temperature (RT) tests; b) -50°C (LT) tests; c) single-lap shear strength values.

Figure 16. The fracture surfaces of single-welded and double-welded samples after the single-lap shear test under RT and LT.

Figure 17. DMA temperature sweeps of resistance-welded CF/PEKK joints (SW90 and DW90): a) storage modulus, E′, RT-start; b) tan(δ), RT-start; c) storage modulus, E’, −50 °C-start; d) tan(δ), −50 °C-start.

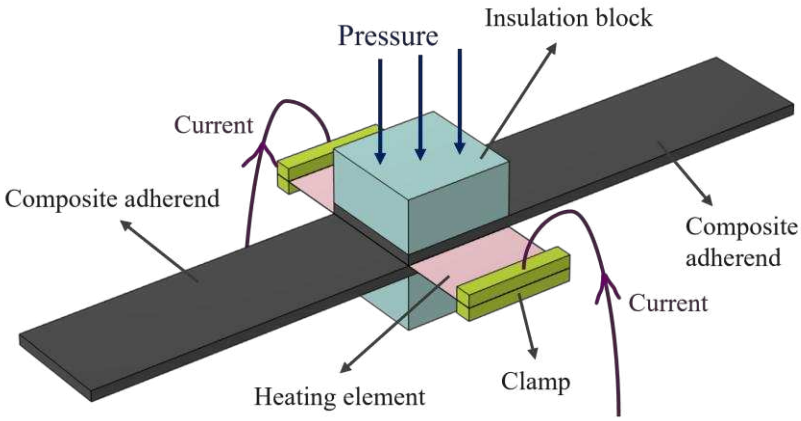

Figure 1. Schematic representation of a typical resistance welding setup.

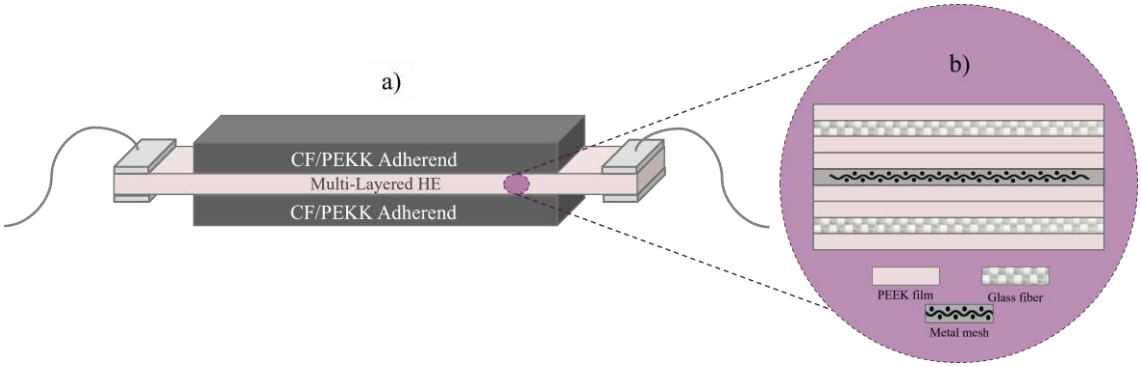

Figure 2. a) Schematic of the multi-layered HE positioned between the CF/PEKK adherends; b) architecture of the fabricated multi-layered HE.

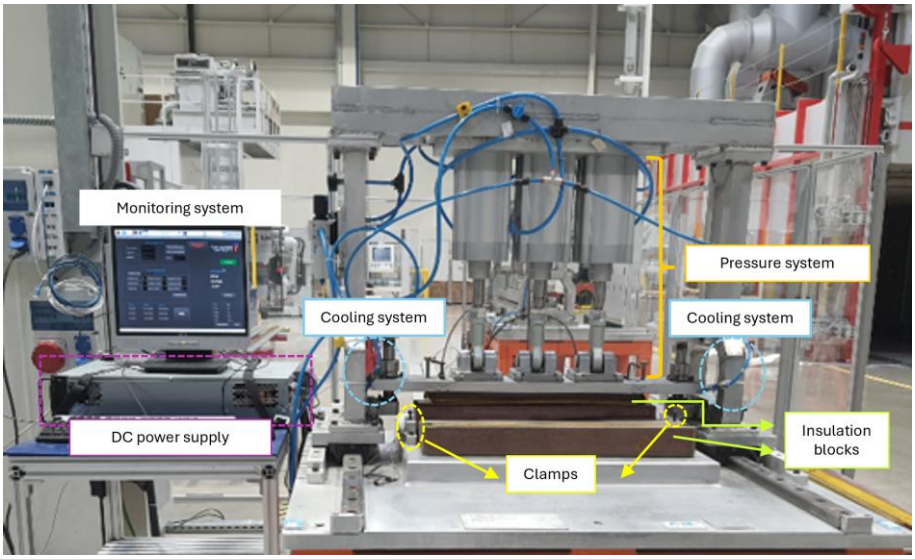

Figure 3. Resistance welding setup configuration.

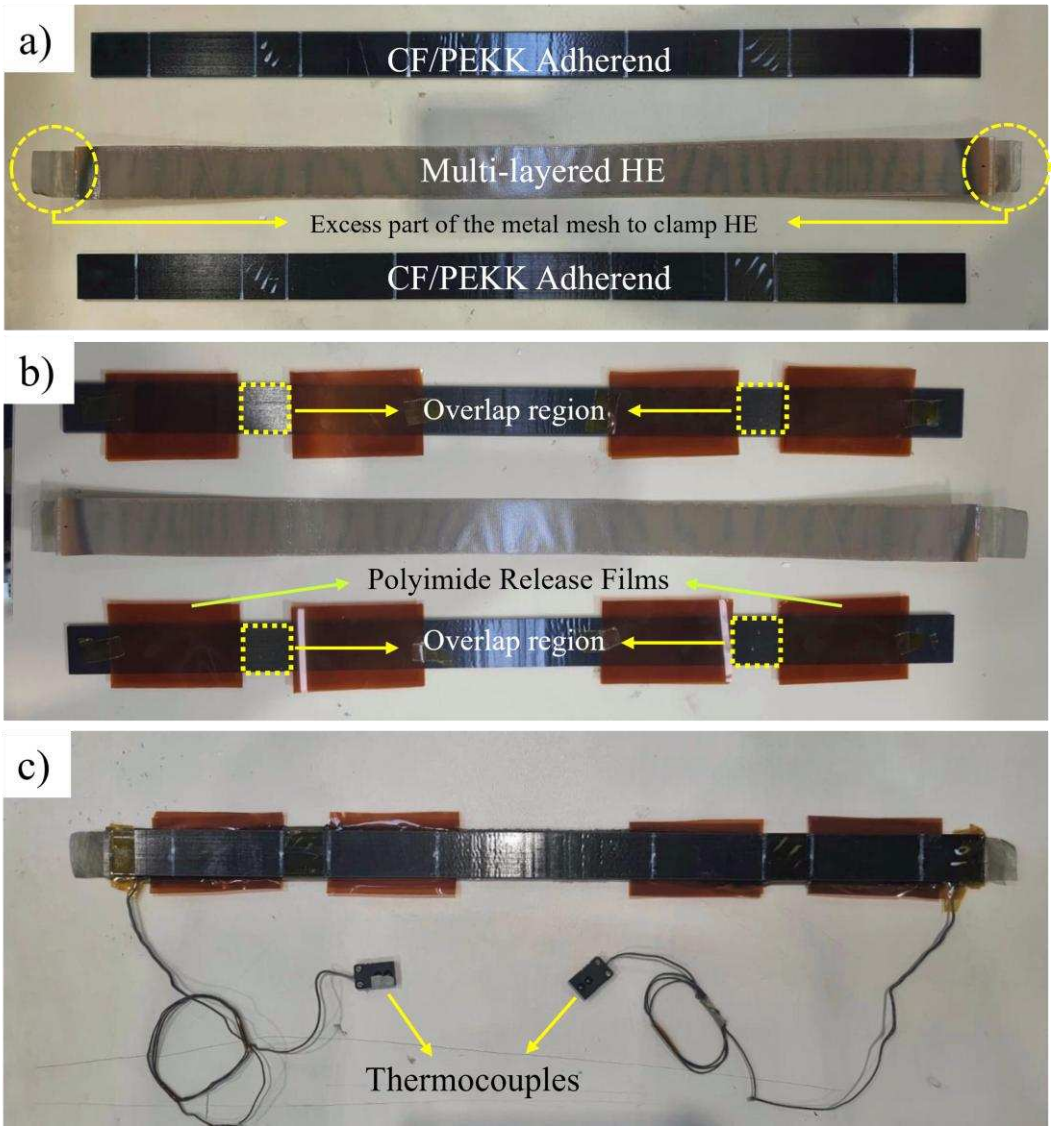

Figure 4. Preparation stages of the welding stack: a) components of the welding stack; b) placement of release film to define overlap regions; c) thermocouple placement.

Figure 5. The single-lap shear test: a) some samples before the test; b-c) SLS fixture; d-e) the sample inside the environmental conditioning chamber; f) the temperature monitoring of the chamber.

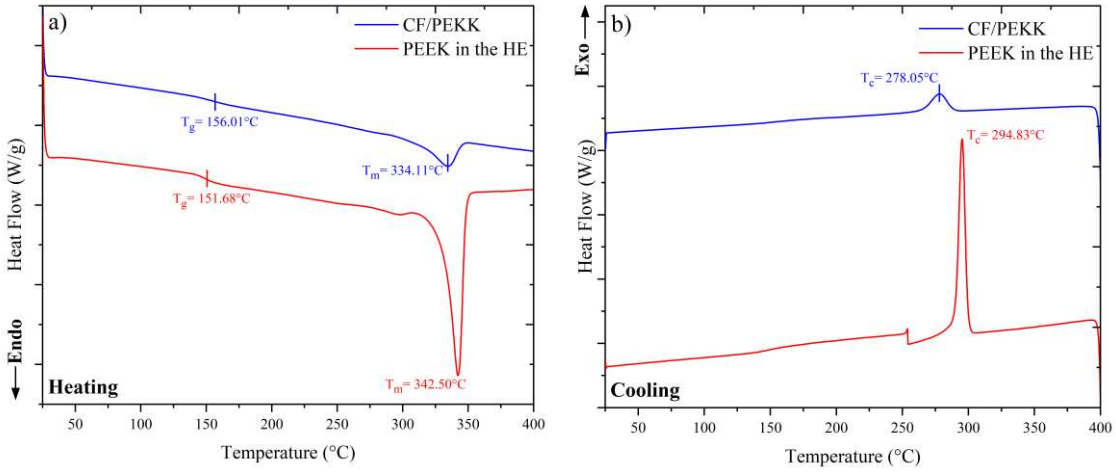

Figure 6. DSC thermograms of CF/PEKK and PEEK of the heating element: a) second heating, b) cooling.

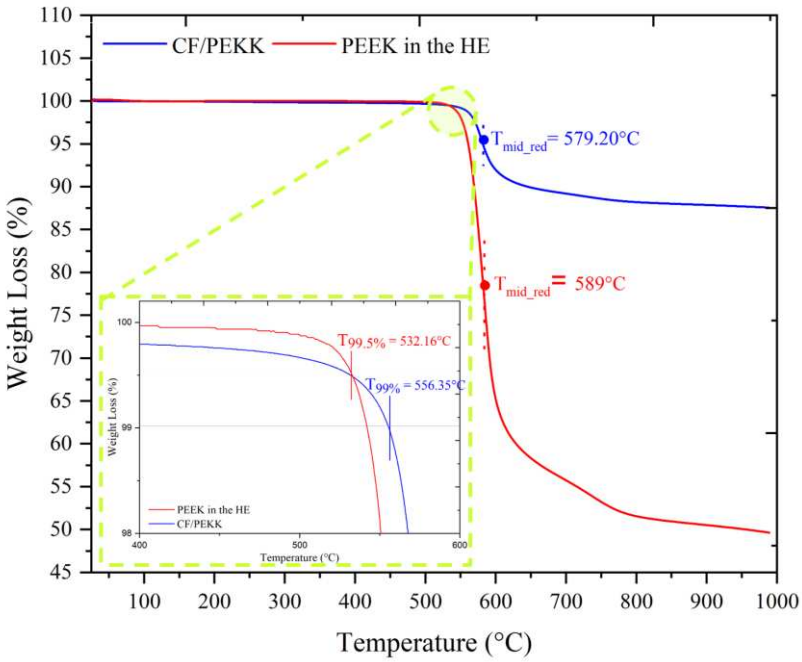

Figure 7. TGA curves of CF/PEKK and PEEK in the heating element.

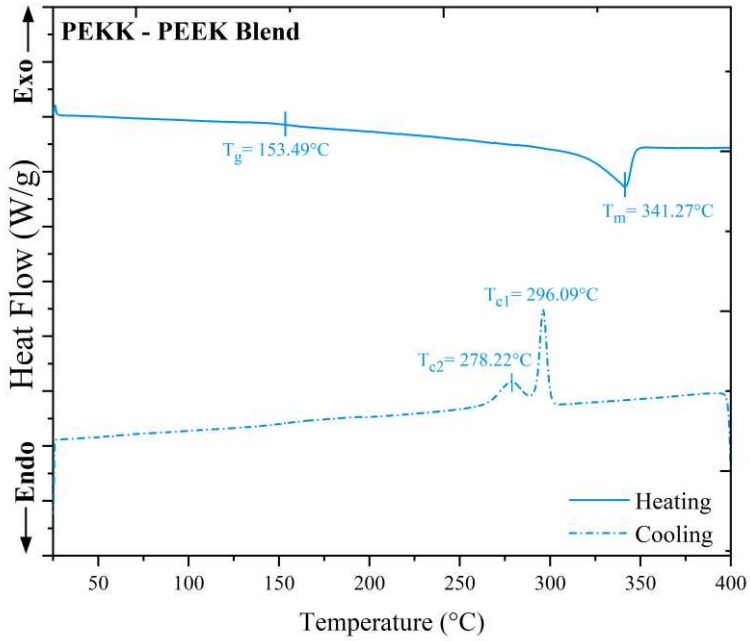

Figure 8. DSC thermogram of the PEKK–PEEK blend prepared from CF/PEKK and the PEEK film in the heating element.

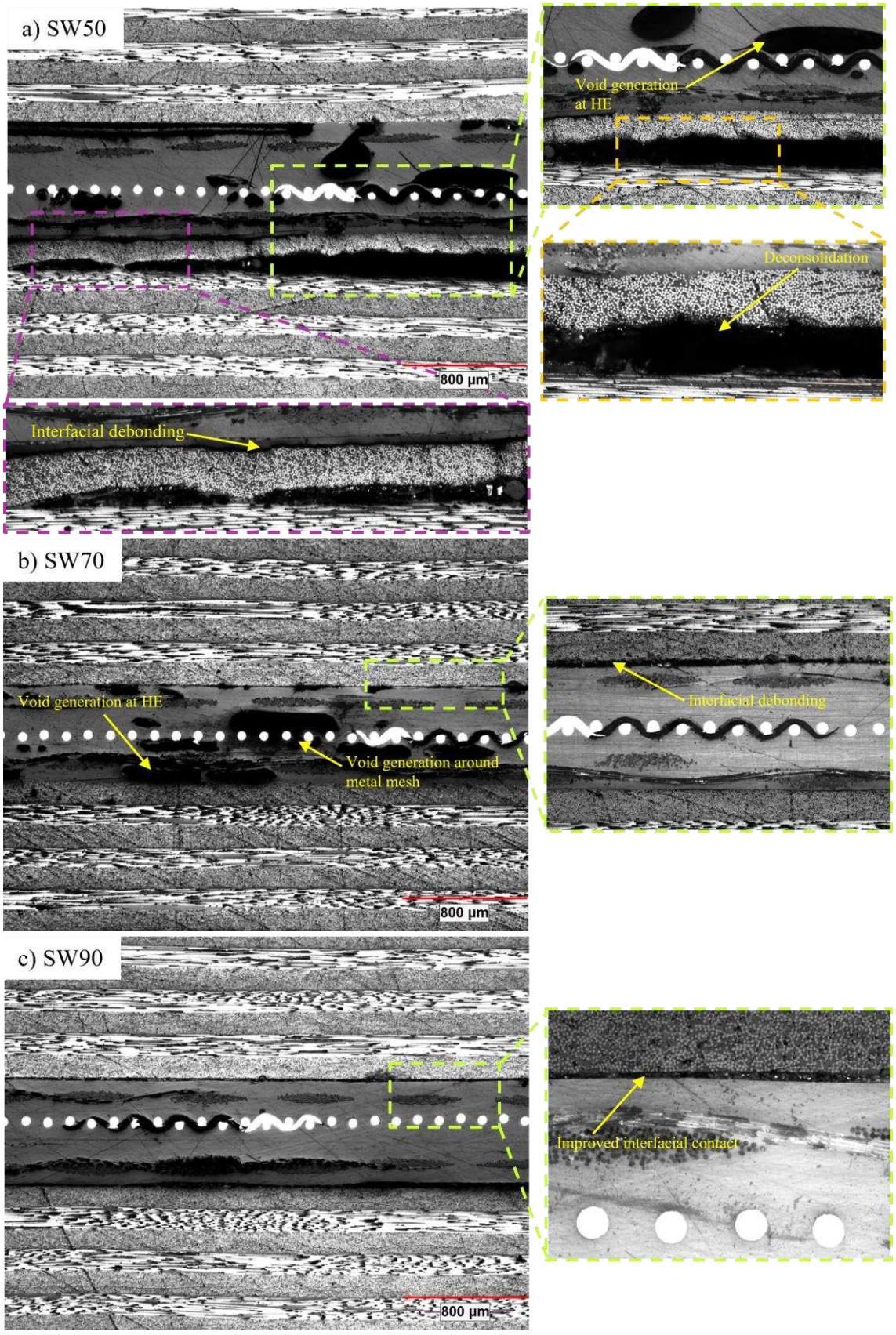

Figure 9. The cross-sectional area investigation through optical microscopy of single-welded samples: a) SW50; b) SW70; c) SW90.

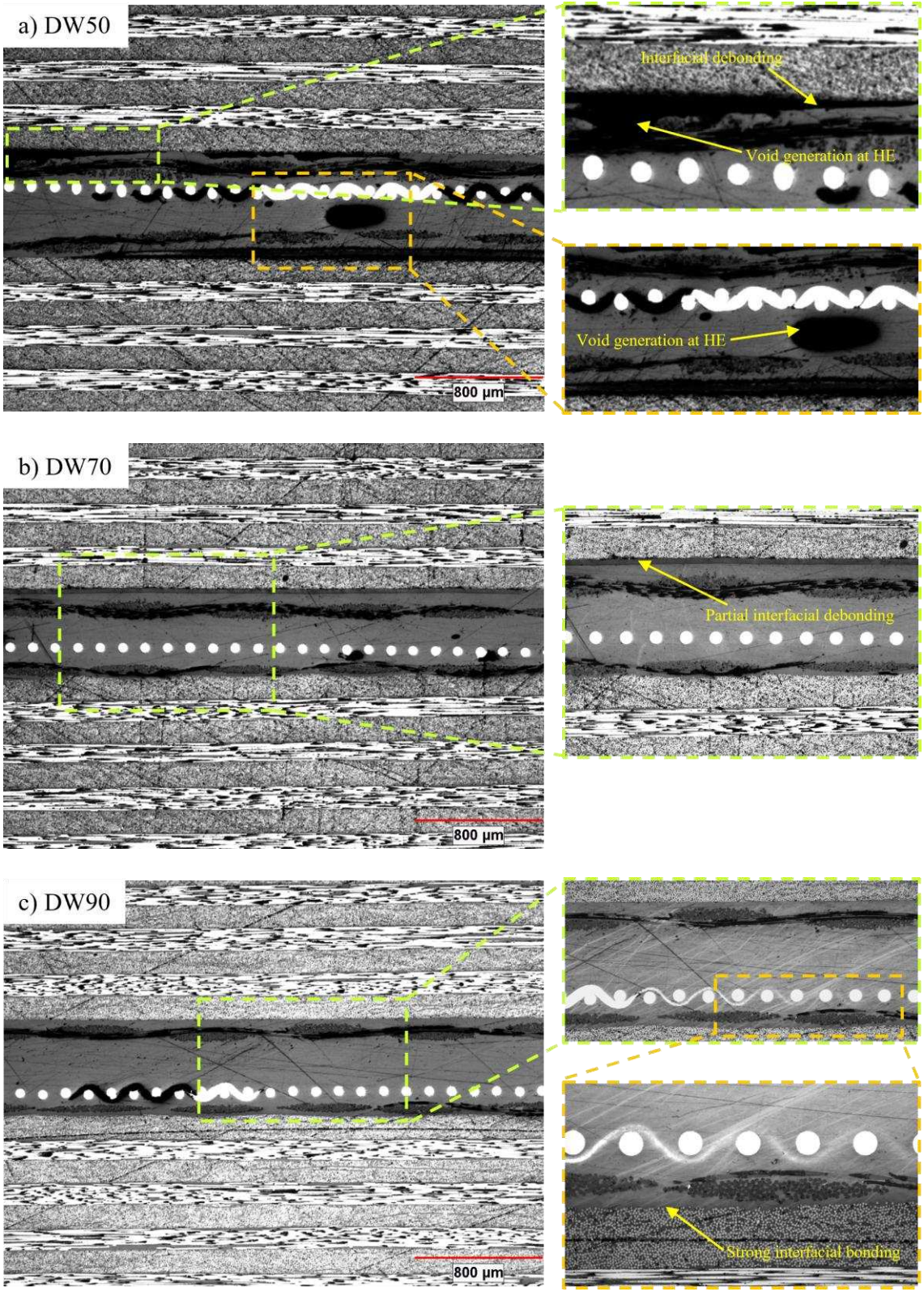

Figure 10. The cross-sectional area investigation through optical microscopy of double-welded samples: a) DW50; b) DW70; c) DW90.

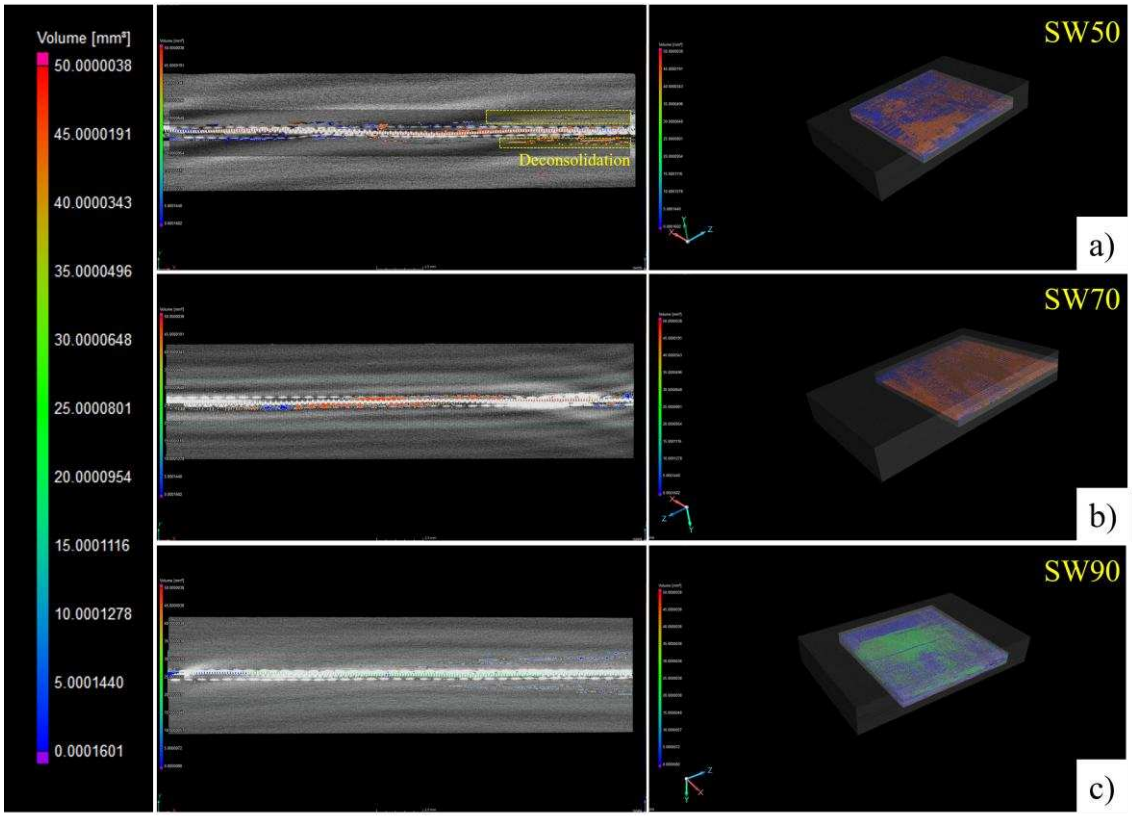

Figure 11. Micro-CT slices and 3D void maps of single-welded composite adherends: a) SW50; b) SW70; c) SW90.

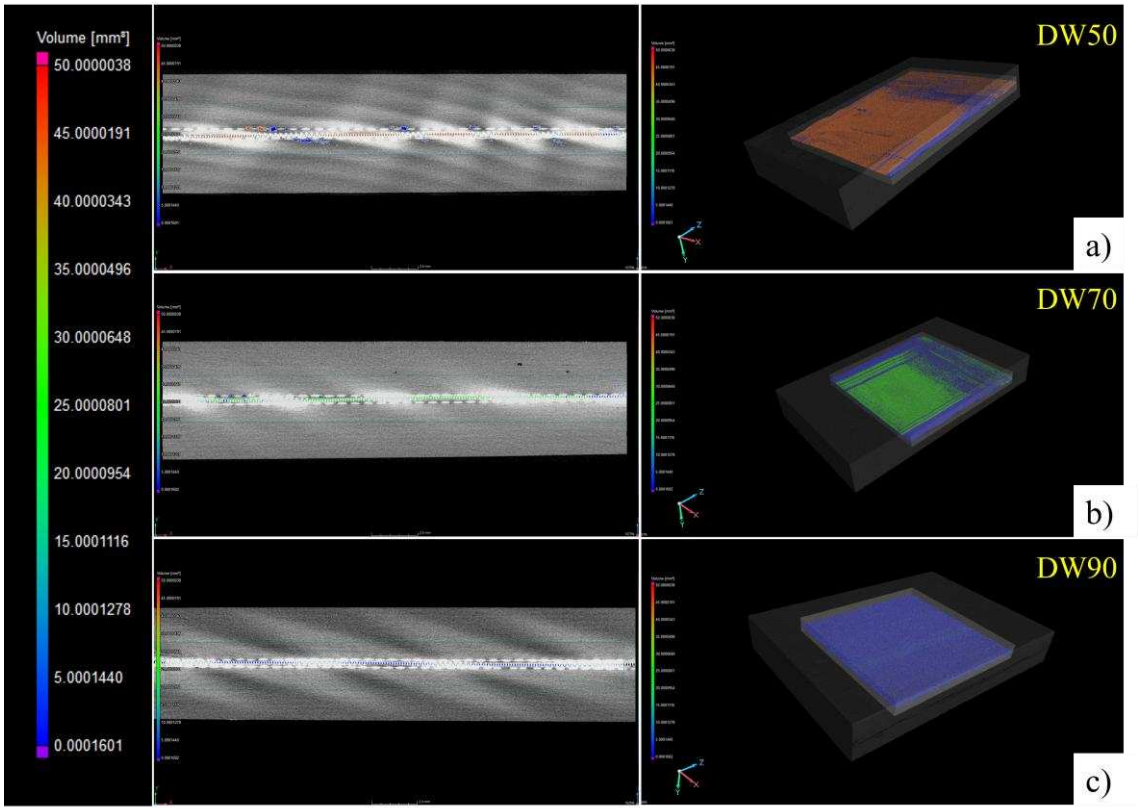

Figure 12. Micro-CT slices and 3D void maps of double-welded composite adherends: a) DW50; b) DW70; c) DW90.

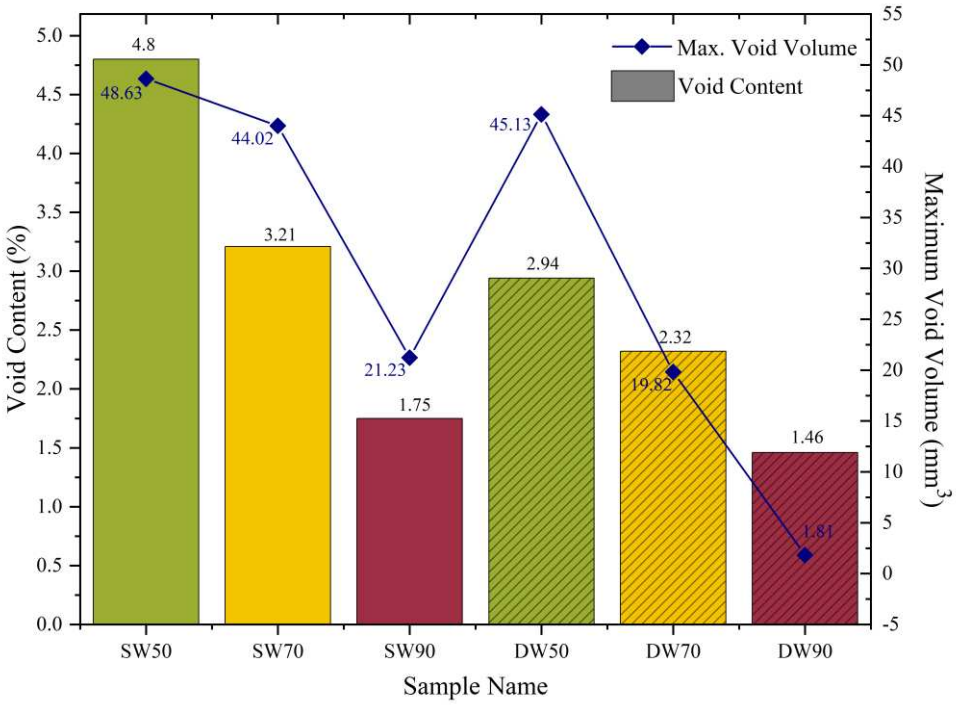

Figure 13. Quantitative void metrics extracted from micro-CT for all welding conditions.

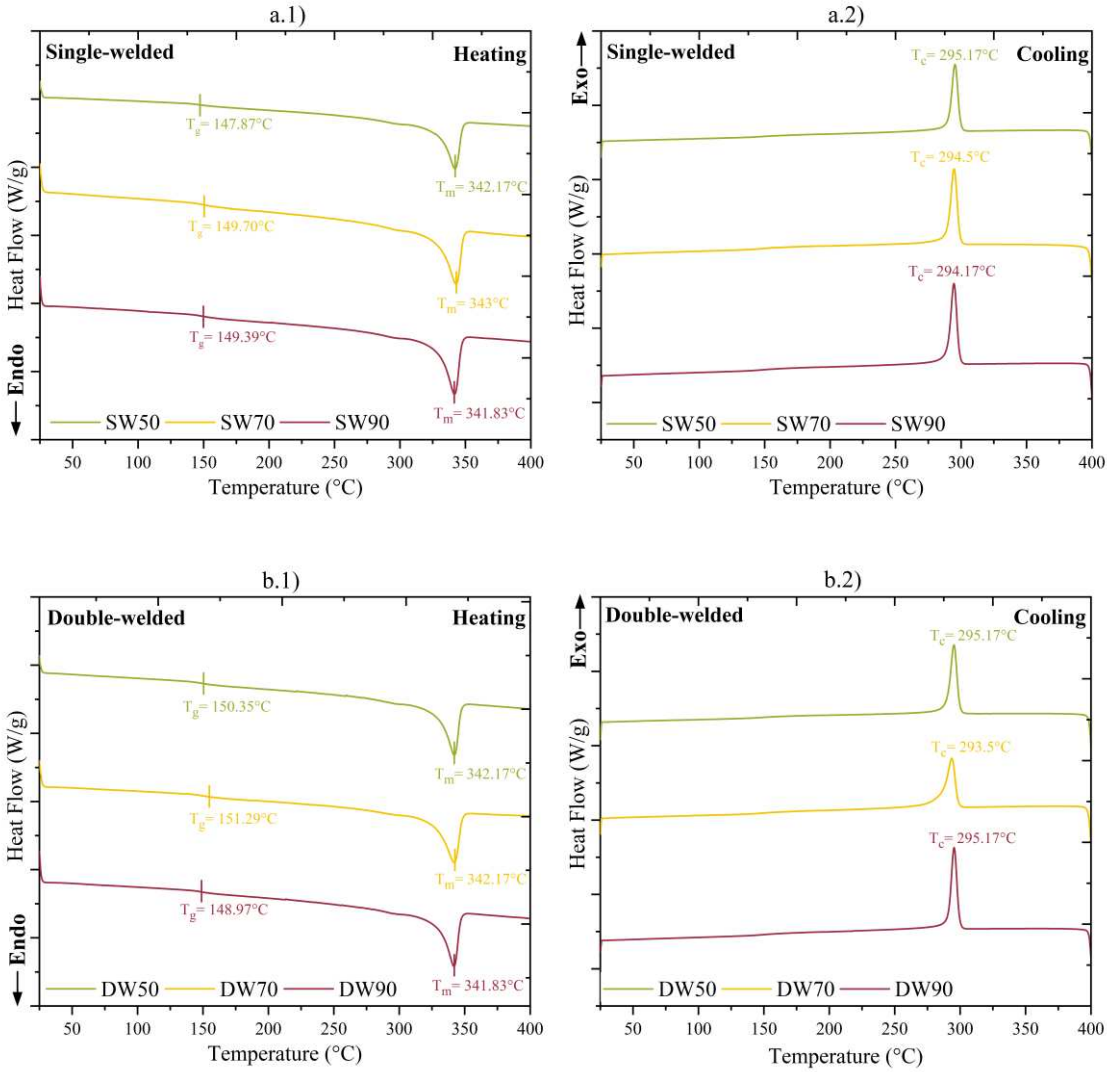

Figure 14. DSC thermograms of polymer bleed-out collected from the overlap region after resistance welding: a.1) second heating profile of SWs; a.2) cooling profile of SWs; b.1) second heating profile of DWs; b.2) cooling profile of DWs.

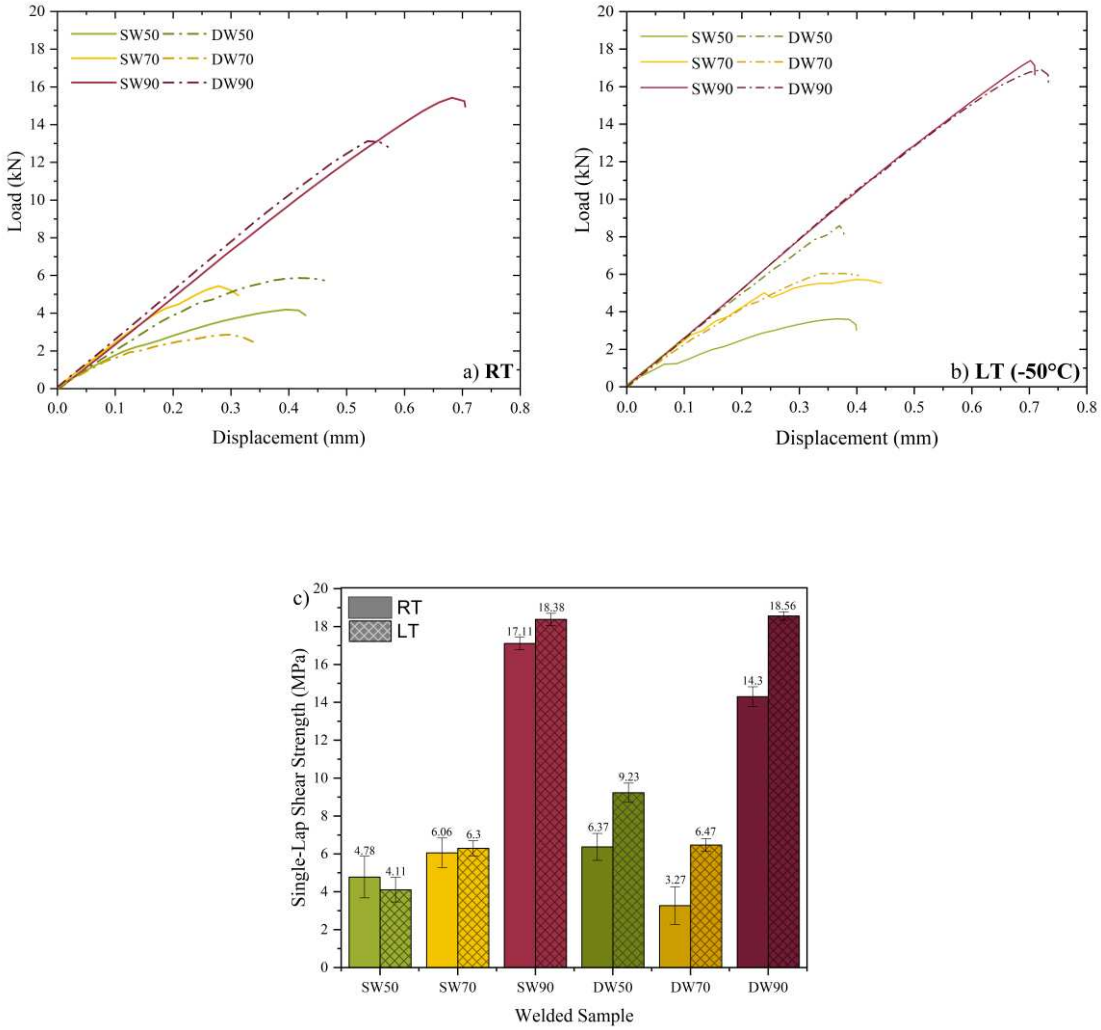

Figure 15. Single-lap shear test results of single-welded and double-welded samples: a) room-temperature (RT) tests; b) -50°C (LT) tests; c) single-lap shear strength values.

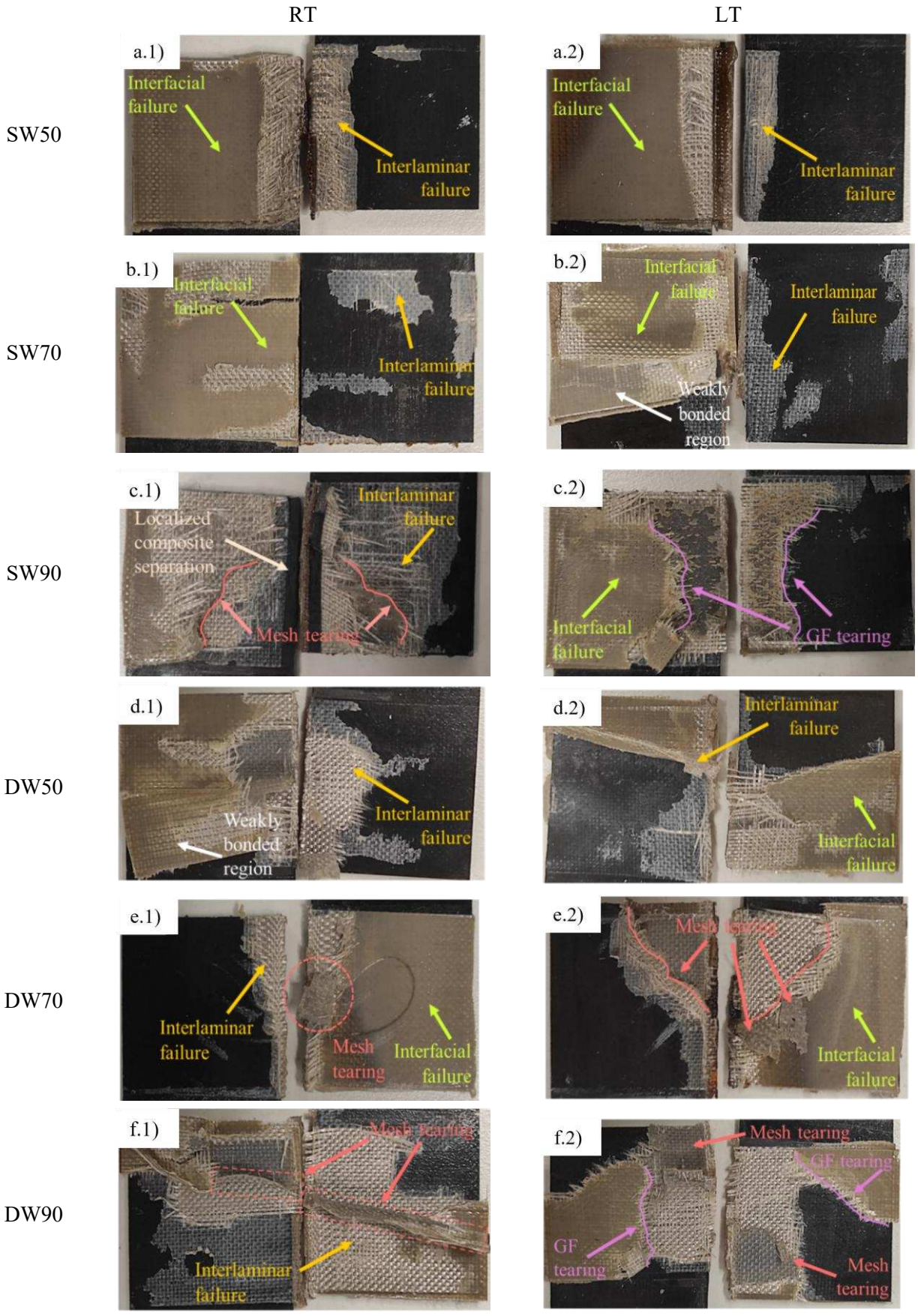
RT
LT
SW50
SW70
SW90
DW50
DW70
DW90
a.1)
Interfacial failure
Interlaminar failure
a.2)
Interfacial failure
Interlaminar failure
b.1)
Interfacial failure
Interlaminar failure
b.2)
Interfacial failure
Interlaminar failure
Weakly bonded region
c.1)
Localized composite separation
Interlaminar failure
Mesh tearing
c.2)
Interfacial failure
GF tearing
d.1)
Weakly bonded region
Interlaminar failure
d.2)
Interlaminar failure
Interfacial failure
e.1)
Interlaminar failure
Mesh tearing
Interfacial failure
e.2)
Mesh tearing
Interfacial failure
f.1)
Mesh tearing
Interlaminar failure
f.2)
Mesh tearing
GF tearing
GF tearing
Mesh tearing

Figure 16. The fracture surfaces of single-welded and double-welded samples after single-lap shear test under RT and LT.

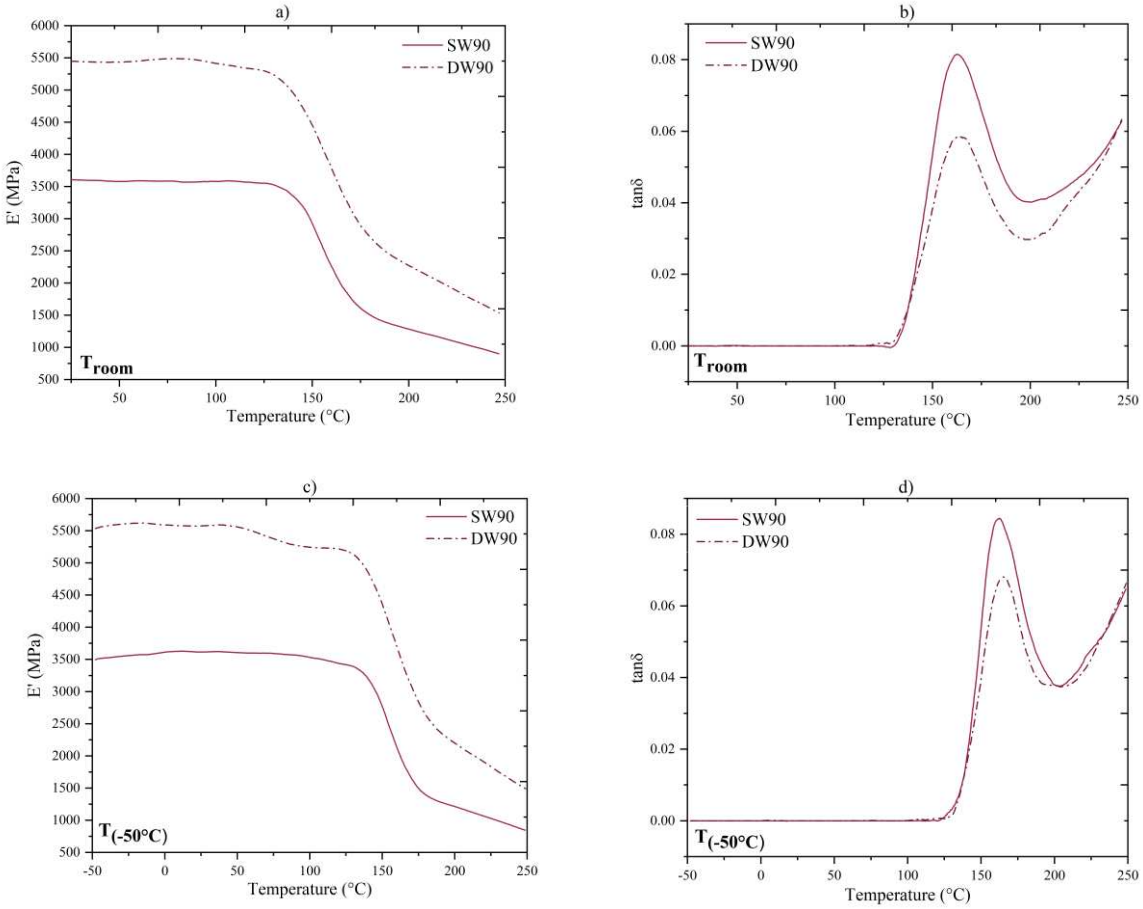

Figure 17. DMA temperature sweeps of resistance-welded CF/PEKK joints (SW90 and DW90): a) storage modulus, E′, RT-start; b) tan(δ), RT-start; c) storage modulus, E', −50 °C-start; d) tan(δ), −50 °C-start.